

Characterisation of influential mechanisms in the life cycle of fog: a study of two extreme events at airports in central-eastern Argentina

Melina Sol Yabra^{A,B,C,*}, Matilde Nicolini^{A,D,E} and Luciano Vidal^B

For full list of author affiliations and declarations see end of paper

*Correspondence to:

Melina Sol Yabra UBA-FCEN-DCAO, Cc1428EGA, Buenos Aires, Argentina Email: myabra@smn.gob.ar

Handling Editor:

Chris Lucas

Received: 6 February 2025 Accepted: 24 July 2025 Published: 29 August 2025

Cite this: Yabra MS et al. (2025)
Characterisation of influential mechanisms in the life cycle of fog: a study of two extreme events at airports in centraleastern Argentina. Journal of Southern Hemisphere Earth Systems Science
75, ES25006. doi:10.1071/ES25006

© 2025 The Author(s) (or their employer(s)). Published by CSIRO Publishing on behalf of the Bureau of Meteorology.

This is an open access article distributed under the Creative Commons Attribution-NonCommercial-NoDerivatives 4.0

International License (CC BY-NC-ND)

OPEN ACCESS

ABSTRACT

Reduced visibility due to fog is a major disruptor of global air traffic, leading to flight cancellations, delays and diversions. To enhance forecasting and mitigate these losses, a thorough understanding of the physical mechanisms governing the life cycle of fog is essential. This study aims to advance this understanding in Argentina, focusing on events where fog simultaneously affected the operations of several airports and, therefore, all the air traffic of the country. Two specific cases, one of extreme duration and one unexpected by forecasters, from different seasons, were analysed using aeronautical meteorological observations (Meteorological Terminal Aviation Report, METAR), radiosondes, Geostationary Operational Environmental Satellite-16 (GOES-16) satellite images and European Centre for Medium-Range Weather Forecasts (ECMWF) Reanalysis (ERA5) reanalysis data. Satellite techniques for detecting low clouds and fog were particularly effective at night but had limitations in distinguishing between fog and low stratus. The study identified multiple mechanisms operating at various scales that contribute to fog formation and dissipation. Both events were characterised by frontal passages – cold in the summer and warm in the winter – accompanied by associated temperature and moisture advections. Various local factors, despite similar synoptic conditions, influenced boundary layer processes at smaller scales, resulting in distinct fog behaviour at each location. These findings highlight the complexity of fog forecasting, fog being driven by multiple interacting processes across different scales, as well as the constraints of current observational systems and numerical models.

Keywords: Argentina, atmospheric observation, aviation, ERA5, fog, forecasting, GOES-16, METAR, meteorology, PBL.

1. Introduction

The World Meteorological Organization (1966) defines fog as a dense mass of small water droplets suspended in the air near the surface that reduces horizontal visibility to less than 1000 m. The phenomenon is called 'mist' when visibility is reduced to between 1000 and 5000 m. Although it can cause complications for many economic and human activities, reduced visibility associated with fog at airports is one of the main disruptors of air traffic globally (Croft 2003). Following safety measures to avoid incidents, cancellation and delay of flights, and diversion to alternative destinations result in substantial economic losses for airlines and airports (Gultepe et al. 2007). In this context, increasing the understanding of the physical mechanisms that govern fog formation, evolution and dissipation could benefit both aeronautical forecasters in operational practice and scientists in developing tools to improve forecasting.

Recently, Lakra and Avishek (2022) reviewed more than 250 research publications about fog and concluded that the complexity of forecasting fog is high owing to multiple processes at different scales playing a role at multiple levels. Attributes such as synoptic conditions, the climatology of an area, stability of the boundary layer, topography and land use are key factors in the fog life cycle. As fog is formed when air approaches

saturation, its formation can be led by a decrease in temperature or an increase in moisture. According to the worldwide literature, radiation fog is the most common type as it is generated by the saturation of air as a result of nocturnal radiative cooling under static stable conditions (Taylor 1917; Pilie et al. 1975; Roach et al. 1976; Meyer and Lala 1990; Roach 1995a; Baker et al. 2002; Haeffelin et al. 2013). Fog can also be generated by the cooling of moist air from below as it moves over a relatively cooler surface or layer of air, and this is called advective fog (Roach 1995b; Baars et al. 2003; Liu et al. 2016). As an example of fog formation led by an increase in moisture, fog can result from the evaporation of precipitation occurring hours earlier, regardless of the mechanism that led to precipitation (frontal, convective, etc.; Petterssen 1969; Tardif and Rasmussen 2007). Another complex process responsible for fog formation is the gradual lowering of the base of low clouds. Regardless of the cause of lowering, it may result from the turbulent transport of cold air and moisture from the radiatively cooled cloud top to its base (Pilié et al. 1979; Cereceda et al. 2002; Keim-Vera et al. 2024). Often, fog occurrence has multiple causes and involves multiple processes simultaneously. In addition to the primary physical mechanisms driving fog formation, its development including dissipation or thinning, as well as deepening or thickening - can be significantly influenced by factors such as turbulence (both thermal and mechanical; Price et al. 2018; Maronga and Bosveld 2017), dew deposition (Li et al. 2021, 2023; Weedon et al. 2024) and cloud cover (Bergot and Guedalia 1994; Guo et al. 2021), among others. Consequently, much research effort worldwide has focused on examining complex fog cases to better understand the interconnected physical mechanisms involved (Price et al. 2015; Hu et al. 2019; Beal et al. 2024; Gandhi et al. 2024).

Despite the considerable disruptions fog causes to aviation in Argentina, research on this phenomenon at the national level has been limited to a few specific regions. Recently, efforts have focused on climatological studies of fog at several major international airports in the country (Schonholz 2015; Ruiz et al. 2018; Lapido 2019; Yabra et al. 2021a, 2023, 2024, 2025). These studies have improved the characterisation of fog hours and events at each airport, providing valuable information on frequency, duration, intensity and persistence of fog events. Findings suggest diverse behaviours likely tied to each airport's geographic location and topographical characteristics. However, given the extensive range of latitudes, climates and topographies across the country, it remains unclear whether distinct physical mechanisms govern fog formation, evolution and dissipation at each site.

For that reason, this study aims to deepen understanding of the mechanisms affecting the life cycle of fog at Argentina's main airports, with a focus on cases where fog simultaneously affected multiple airports, leading to significant operational challenges. The goal is to identify the mechanisms driving fog formation, evolution and dissipation, as well as its spatial and temporal variability, through two detailed case studies. Key motivating questions include:

- Is the same main physical process simultaneously affecting the entire study region?
- · How much do local factors influence fog formation?
- Can similar synoptic conditions produce different types of fog?
- Do synoptic and boundary layer mechanisms interact with or counteract each other, and which is decisive for fog formation or dissipation?

To explore these questions, surface and upper-air observations are used, supplemented by European Centre for Medium-Range Weather Forecasts (ECMWF) Reanalysis (ERA5) reanalysis data sets (Hersbach *et al.* 2020), to study atmospheric circulation at higher altitudes and analyse planetary boundary layer (PBL) behaviour, after thorough validation of data agreement.

In addition to fog formation, the evolution and dissipation processes of fog are also of great importance for aeronautical activity, as they are also implicated in modifications to flight plans. In this regard, satellite images constitute an observational tool capable of representing and monitoring the state of the atmosphere and its evolution. This resource is the most used by aeronautical forecasters in Argentina (Yabra et al. 2021b), particularly the Geostationary Operational Environmental Satellite-16 (GOES-16) satellite, which has been operationally capturing the entire Argentine territory since 2017 (Schmit et al. 2017). Worldwide, various techniques for fog identification using some of its 16 bands have already been studied, yielding promising results, especially during night-time hours (Gultepe et al. 2021). However, radiation reflection during daytime hours and high clouds overlaying fog may limit its use. Therefore, the second objective of the present study is to evaluate the correlation between satellite information and surface observations for two fog events in Argentina by identifying fog from satellite images and products that have already been used in other countries (Amani et al. 2019) in order to validate them as a fog observational tool.

This research article is organised as follows. In Section 2, the study periods and airports are detailed, and in Section 3, the data sets used are presented. The calculation of variables of interest and fog detection techniques based on satellite information are described in Section 4. Section 5 describes a validation of the reanalysis data set by comparing it with surface and upper-air observations. The analysis of the mechanisms involved in the first fog case (July 2020) is addressed in Section 6 and is divided into three parts: synoptical conditions, satellite images and local processes. Similarities and differences found in the January 2023 case with respecto to the first are discussed in Section 7. In Section 8, results are discussed and synthesised, and the conclusions of the work are presented.

2. Study cases

The case studies chosen for this work correspond to fog events that occurred on 18 July 2020 and 27 January 2023 in the central-eastern region of the country. Both cases were selected because they involved extensive fog cover that affected several of the country's major airports and because of the difficulties in forecasting both its formation and dissipation.

Within the study region, the main airports that could have been affected by this phenomenon were selected: Ezeiza, Aeroparque, Rosario, Córdoba, Mar del Plata in Argentina, and Montevideo in Uruguay (Fig. 1). Although the study area is sited in Argentina's central region, it includes varied terrain - mountains to the west near Córdoba, plains in the middle, a coastal area near Mar del Plata, and riverine regions close to Aeroparque and Montevideo. Climatological studies indicate that all airports exhibit a monthly and diurnal fog cycle, with peak occurrences in fall (autumn) and winter during the night and around dawn with very light and calm winds (Yabra et al. 2023, 2025). The exception is Aeroparque, where fog lacks a consistent time pattern but is more frequent in winter, likely owing to its proximity (less than 100 m) to the La Plata River, making it more susceptible to advection fog or the advection of fog already formed over the river (Vasques Ferro and Ribero 2015; Yabra et al. 2021b). By contrast, Ezeiza airport, located ~40 km inland, exhibits our first mentioned climatological occurrence frequency. Mar del Plata and Montevideo airports, also located near coastlines (~4 and ~3 km away respectively) with urbanised areas in between, show fog characteristics primarily associated with radiative processes.

Following the fog event identification criteria of Yabra et al. (2025), these events can be classified as extreme based

on their duration (more than 13 h) and median visibility (400 m). This is the case for Ezeiza airport during the first selected study case, with a 29-h duration and 370-m median visibility. Airports like Aeroparque and Mar del Plata do not fall into this class owing to their visibility reduction, with medians of 1302 and 926 m respectively, although they had durations of 23 and 15 h respectively. However, stretches of several hours in the fog events fall under the Low Visibility Procedures (LVP; International Civil Aviation Organization 2023) category, as the visibility dropped below the minimum thresholds, which vary depending on the airport, operations and flights. This signifies the inability to land or take off, leading to flight cancellations, delays or diversions to alternative airports. The selected airports are the most frequently used alternatives for each other when the primary airport is operating under LVP conditions. In this context, fog affecting most of these airports poses a significant challenge for Argentina's aviation operations. Information on the effect that the first event had on aviation activity in the region is available but, owing to the significant restrictions imposed in response to the COVID-19 pandemic during 2020, the value of this information is limited. This event raises questions such as:

- What mechanisms contribute to the prolonged duration of a fog event?
- How can two closely situated airports experience different fog evolution patterns?

The January 2023 case lasted for a shorter period (6 h) but strongly affected aviation operations at Ezeiza Airport. The severity of the impact was increased by the lack of anticipation of visibility reduction in the forecast, which should have

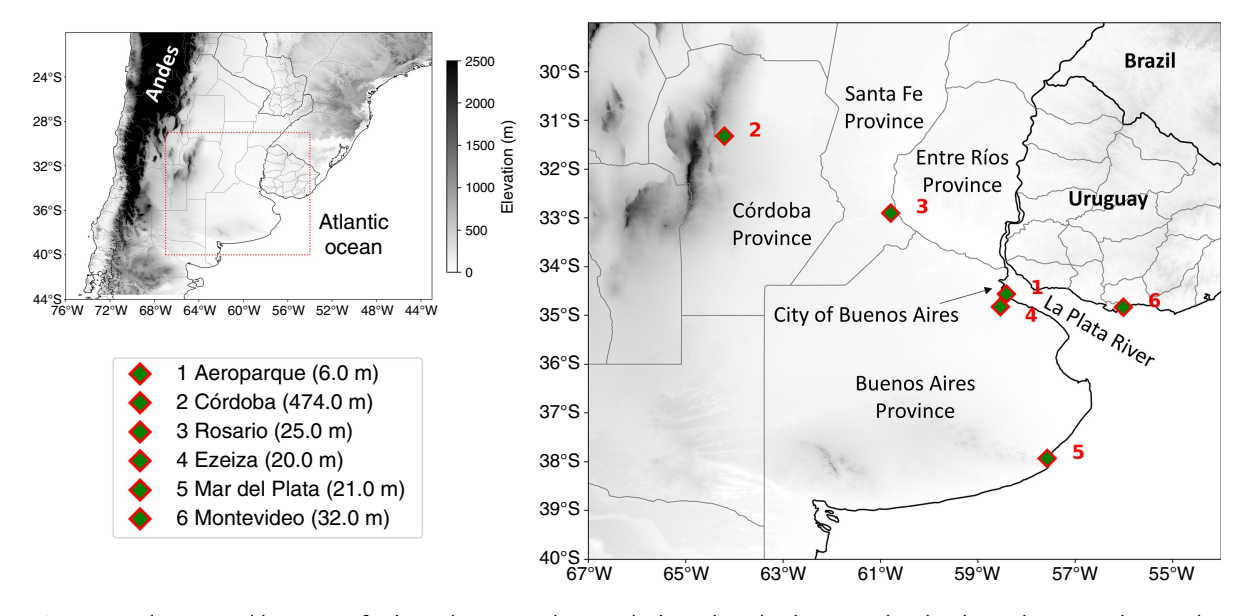


Fig. 1. Study area and location of selected airports along with their altitude above sea level indicated in parentheses. The topographic information comes from the Digital Elevation Model (DEM) and HydroSHEDS from the SRTM mission (NASA Shuttle Radar Topography Mission) (Rodriguez *et al.* 2005) with a horizontal resolution of 90 m.

been predicted 24 h before (International Civil Aviation Organization 2016), as it occurred during the austral summer, a season when fog is a climatologically rare event over the selected airports (Yabra *et al.* 2023, 2025).

3. Data

To achieve the objectives of this work, surface and upper-air observations, satellite images and reanalysis data sets were used and are described below. The study area and the selected airports can be seen in Fig. 1, and the study periods cover 00Z 17 July 2020 to 23Z 19 July 2020 for the first case, and 00Z 27 January 2023 to 23Z 29 January 2023 for the second case.

3.1. Hourly in situ observations

For this study, hourly aeronautical meteorological reports (Meteorological Terminal Aviation Report, METAR) from the selected airports (Fig. 1) were used during both periods. Once decoded, the values of the following meteorological variables were extracted: air temperature, dew point temperature, visibility, wind speed and direction, present weather, QNH (barometric pressure adjusted to sea level), cloud cover and cloud base height at three levels. Considering the hourly resolution of these observations, an airport with 100% data coverage would have a total of 72 observations for each event. This is the case for Montevideo, Ezeiza, Córdoba and Rosario. Of the remaining airports, Aeroparque has 98.6% data available and Mar del Plata has 95.8%.

3.2. Radiosonde observations

Upper-air *in situ* measurements from radiosondes provide essential validation for the reanalysis data set at different altitudes. For the fog events studied, Córdoba is the only station that launched radiosondes during the first event. Consequently, in this analysis, the wind and thermodynamic vertical profiles from 12:00 hours UTC at Córdoba were obtained from the Wyoming Weather Web. These profiles are examined in Section 5 to assess the alignment between the observed data and reanalysis outputs.

3.3. Reanalysis

To study the synoptic, mesoscale and PBL processes that might be influencing the life cycle of fog in the study cases, ERA5 reanalysis data from the European Centre for Medium-Range Weather Forecasts (ECMWF) was utilised (Hersbach *et al.* 2020). This reanalysis data set has already been used in similar studies of fog to analyse synoptic and mesoscale processes in other regions (Andersen *et al.* 2020; Zhao *et al.* 2020). Because it combines model data with observations from different sources around the world, its local representativeness would depend in part on the density and number of available observations to be assimilated. It

has a horizontal resolution of $0.25 \times 0.25^\circ$, a temporal resolution of 1 h and a vertical resolution of 25 up to 750, 50 up to 500, and 100 hPa up to the top of the model domain. Although this reanalysis provides the highest resolution available for the region (\sim 25 km), it may still fall short in capturing topographic or very local effects. Consequently, the analysis of turbulent fluxes (model parameterisations) and PBL processes presented in Section 6 serves as a qualitative approach for the actual mechanisms, whose study remains challenging owing to the lack of accurate observational data (with higher temporal and spatial resolution, among other requirements).

The data were collected for both study periods. The variables extracted from this data set include temperature, geopotential height, zonal, meridional and vertical wind components, specific humidity, relative humidity and liquid water content. Additionally, variables at specific levels were extracted, such as air temperature and dew point temperature 2 m above the ground, zonal and meridional wind components 10 and 100 m above the ground, surface sensible and latent heat flux, cloud base height and friction velocity. The cloud base height was estimated by identifying, from the second lowest model level, the height at which the cloud fraction exceeded 1% and the liquid water content exceeded 1×10^{-6} kg kg⁻¹ (Hersbach et al. 2020). The fog identified by the model at the lowest level is not considered when defining cloud base height. Regarding surface heat flux, according to the conventions of the ECMWF, vertical fluxes directed downward are expressed as positive numbers.

3.4. Satellite observations

To achieve the final objective of this work, satellite observations from the NOAA and NASA geostationary satellite GOES-16 were used. In this work, data from the Advanced Baseline Imager (ABI; Schmit et al. 2017) sensor are used, which provides images every 10 min from 16 spectral bands with spatial resolutions ranging between 0.5 and 2 km. Specifically, Channels 2 (0.64 μm ; visible), 7 (3.9 μm ; shortwave infrared), 13 (11.3 μm ; 'clean window' thermal infrared) and 15 (12.3 μm ; 'dirty window' thermal infrared) from the Level 2 product were employed, all with 2-km spatial resolution. An explanation for choosing these wavelengths is addressed in the following section.

4. Methodology

METAR can include information on cloud cover and cloud base height corresponding to any of three different vertical levels. Consequently, METAR may provide information on mid and high-level clouds while omitting information on low-level clouds if none are present. To synthesise this information and ensure consistency with satellite images and reanalysis data, a combination of these three levels was used. For cloud cover, total coverage is defined as the

highest value among the three reported cloud cover levels. For the cloud base height, the absolute base is defined as the lowest value among the three reported heights.

Whereas most of the variables used were obtained directly from observations or reanalysis data, some variables were derived from these for specific analyses. This is the case with specific and relative humidity, potential, equivalent potential temperature, and advections of temperature and specific humidity. Another variable used in this work is the Modified Richardson (MRi) number introduced by Baker *et al.* (2002) for fog forecasting purposes, calculated as:

$$MRi = \frac{T - T_0}{V^2}$$
 (1)

where T is the temperature (°C) and and V is the wind speed (knots) at the first vertical level of the model (1000 hPa) or the first level above surface pressure if it is lower than 1000 hPa, and $T_{\rm o}$ is the temperature 2 m above ground level (°C). This quantity is used to represent dynamic stability and turbulence in a layer immediately above the surface. Although the former authors used the thresholds 0.025 and 0.04 to classify the boundary layer as mixed, neutral or stable, in the present study, the temporal evolution of this parameter is qualitatively evaluated and related to sensible heat flux and friction velocity variations.

To address the final proposed objective, different images and products were used for fog detection using satellite information: two valid for night-time and one for daytime hours. The first product evaluated has been commonly used for the detection of fog and low stratus (without being able to distinguish between them) (hereafter FLS) for several decades (Eyre et al. 1984; Cermak and Bendix 2007). This product uses the brightness temperature difference (BTD) between the 11.3and 3.9-um wavelengths (Band 13 and Band 7 from ABI). FLS is used at night to identify clouds composed of water droplets. These clouds do not emit shortwave radiation at 3.9 µm like a black body would, but they do emit longwave (infrared, IR) radiation at 11.3 um. Therefore, low stratus or fog shows positive values in this BTD. This product has a strong limitation during daytime hours as the 3.9-µm band contains a daytime solar reflectance component. The second technique is the red-green-blue (RGB) composite called Nighttime Microphysics, which combines three channels of the ABI sensor (IR 3.9, IR 11.3 and IR 12.3 μm) and uses three components as input: (1) the BTD (IR 12.3-IR 11.3 µm) to help distinguish thick clouds from thin clouds, (2) the FLS product to help separate fog or low water clouds from the surrounding cloud-free surface, and (3) the IR 11.3-µm channel to help separate dense clouds according to their top temperature. It should be noted that the Nighttime Microphysics RGB (hereafter 'RGB') product may not detect the fog or low stratus layer if it is extremely thin or if it is covered by higherlevel clouds (e.g. cirrus). Also, as it uses the FLS product, it has the limitation mentioned during daytime hours. Table 1

Table 1. Meaning of the colours found in RGB composition image.

| Colour | Description | Colour | Description |
|--------|--------------------------------|--------|------------------------------|
| | Fog | | High, thin, ice cloud |
| | Very low, warm cloud | | High, very thin, ice cloud |
| | Low, cool, cloud | | High, thick cloud |
| | Mid water cloud | | High, thin cloud |
| | Mid, thick, water or ice cloud | | High, thick, very cold cloud |

describes the different types of clouds that can be distinguished with this product according to the colour shown. The third technique is based on the analysis of images in the visible range (Band 2, 0.64 μ m; hereafter VIS) during daytime hours. In these images, low clouds (stratus or fog) appear smooth (not textured) and with shades ranging from white to grey, depending mainly on the size of the water droplets (albedo) and the time of day (sunlight reflection).

5. Validation of ERA5 against in situ observations

To draw accurate conclusions about atmospheric behaviour during the fog events based on reanalysis data, it is essential to first validate these data for both surface and upper-air levels. For the initial case study, a temporal comparison of selected reanalysis variables with observations from METARs and radiosondes at Córdoba airport was conducted, shown in Fig. 2 and 3 respectively. This airport was chosen owing to its complete data availability and its location in complex terrain, providing an opportunity to evaluate the impact of coarse spatial resolution on the analysis. It is important to note that these data sets are not entirely independent as METAR and radiosonde observations should be assimilated into the numerical model to create the reanalysis data set (Hersbach *et al.* 2020).

For surface validation (Fig. 2), dew point and air temperatures show good agreement between ERA5 data and observations on the first day of the analysis although there is underestimation of the maximum northern wind speed. However, by fog onset at this station (04Z on 18 July), both temperatures are overestimated, and there is a discrepancy in wind direction. This discrepancy could be attributed to the reanalysis' inability to accurately represent the orography north of the station (see Fig. 1), which acts as a mechanical barrier to northerly winds at lower levels. From vertical profiles, it can be seen that there is no strong disagreement in wind variables during the 3 days other than a slight underestimation of wind speed maxima (Fig. 3). The northern wind at the surface, absent in observations during 18 July, may explain the overestimated dew point temperature (Fig. 2). On the final day of the analysis, discrepancies in wind direction and speed also result in an overestimation

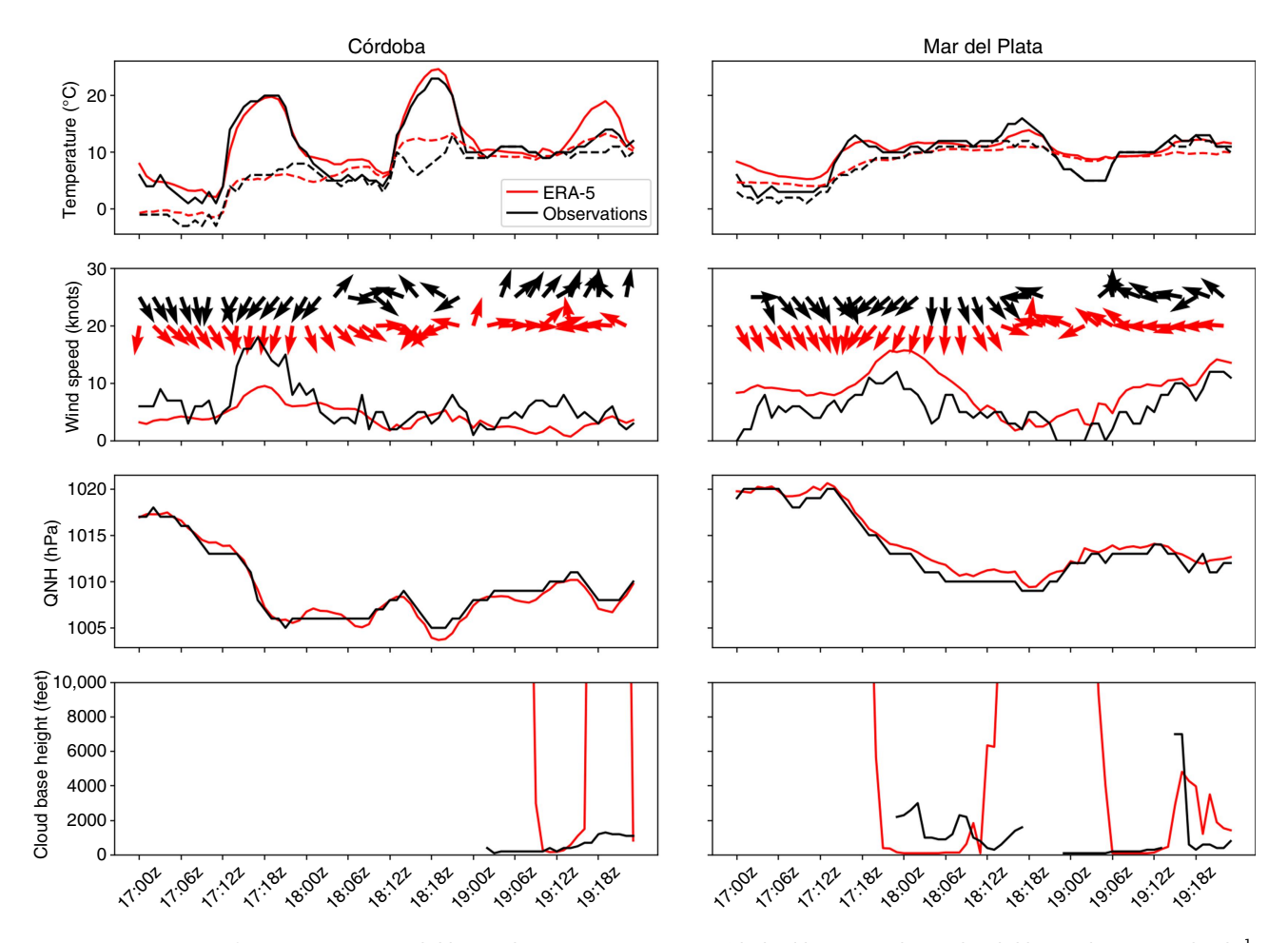


Fig. 2. Time series of air temperature (solid lines), dew point temperature (dashed lines), wind speed (solid lines, 1 knot = 1.85 km h^{-1}) and wind direction (normalised vectors), QNH and cloud ceiling (1000 ft = ~305 m) at Córdoba (first column) and Mar del Plata airport (second column) using METAR data (in black) and ERA5 reanalysis data (in red) for the study case of July 2020.

of daytime temperatures. Discrepancies emerged for ERA5 cloud base height showing that when this information is present in the METAR (only included when it could affect the air traffic; International Civil Aviation Organization 2016), the estimation of cloud base height is strongly influenced by this information. When no information is available for its assimilation, the cloud base is estimated purely based on its definition using fixed thresholds for liquid water content and cloud fraction (Hersbach et al. 2020). These thresholds may be too large, leading to a significant overestimation of cloud base height during the times without available information. Additionally, because clouds in ERA5 reanalysis are modelled, their accuracy is contingent on the microphysics parameterisations employed. Although the thermodynamic profiles (Fig. 3) showed close agreement in air and dew point temperatures at cloud base and inversion height, discrepancies in cloud base height may stem from the meteorological observers' limitations in visually estimating cloud ceilings during night-time or foggy conditions.

To extend the surface validation to other stations that might not be affected by the poor representation of complex

terrain, a similar surface analysis was performed for Mar del Plata Airport (Fig. 2), which is situated on flat terrain but near the sea coast. Unlike Córdoba, Mar del Plata airport shows an overestimation of northern wind speeds on 17 and 18 July. This leads to a slight overestimation of both dew point and air temperatures during 17 July and the transition between 18 and 19 July, though there are no clear differences in relative humidity content. Additionally, the reanalysis shows good agreement with observations across all variables on the final day of the first case study.

For the second fog case, a similar analysis – not shown – indicated analogous findings to the first case. However, it highlighted an overestimation of wind speed during periods when calm conditions were recorded in observations.

6. Case study: July 2020 fog event

6.1. Synoptic setting and evolution

Fig. 4 and 5 show the evolution of atmospheric circulation at the synoptic scale. From these figures, the conditions at fog

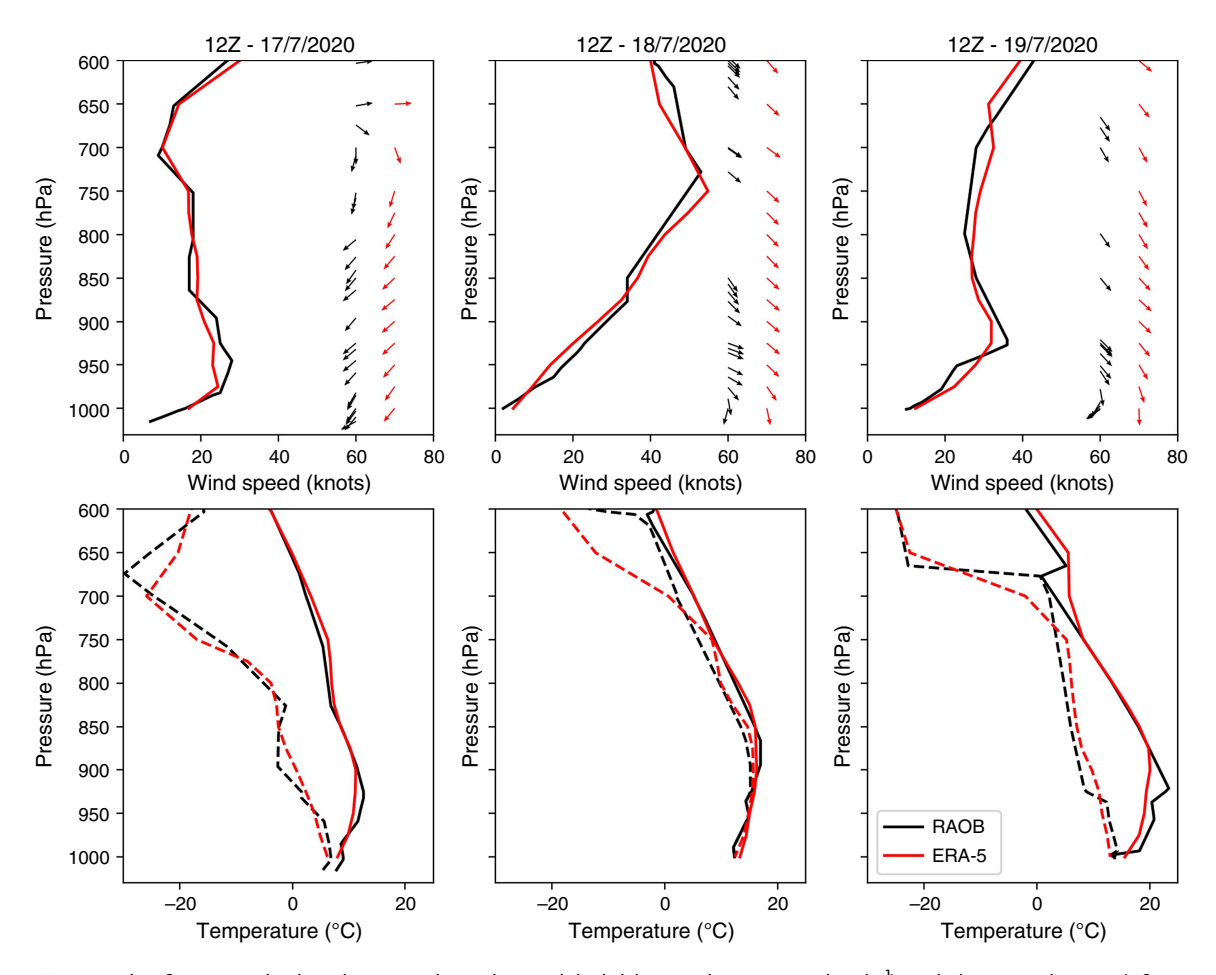


Fig. 3. The first row displays horizontal wind speed (solid lines, 1 knot = 1.85 km h^{-1}) and direction (vectors) from radiosonde observations (RAOB, shown in black) alongside ERA5 reanalysis data (in red) at Córdoba airport. Similarly, the second row presents the vertical profiles of air temperature (solid lines) and dew point temperature (dashed lines) for comparison. Pressure levels (hPa) are shown on the vertical axis; approximate height above mean sea level is 1000 hPa = ~0 m, 850 hPa = ~1500 m, 700 hPa = ~3000 m, 500 hPa = ~5500 m.

onset show a warm frontal zone slowly moving southward. This front is primarily sustained by the South American Low-Level Jet (SALLJ; Campetella and Vera 2002; Yabra et al. 2022) and by the anticyclonic circulation in the Atlantic Ocean at latitudes between 25 and 35°S (Fig. 4), which induces a north-north-east flow at low levels on its western side. The position of the baroclinic zone at 850 hPa relative to the same zone at 975 hPa further north (Fig. 4a, c) allows inference about the inclination of the frontal surface where warm air overlaps relatively cooler air. It can be seen that this front has strong warm advection behind it (Fig. 5a) and slight moisture advection (Fig. 5g) promoted by the large temperature and humidity difference between the two air masses (Fig. 5d, j). At high levels, an increase in the upper-level jet speed in the country's central region coincides with the presence of the baroclinic zone at lower levels due to the thermal wind relationship (Fig. 4e).

At the start of the event (06Z on 18 July), the warm front began to cross the study region. Fig. 5d shows that at that

time, the airports of Ezeiza, Aeroparque, Córdoba and Rosario were still immersed in the cold air mass near the surface. However, their humidity began to increase, transitioning to that of the warm air mass (Fig. 5j).

The cold and dry air mass in the south of the country began to be fed by the southerly flow formed as a consequence of the eastward displacement of a low-pressure centre at mid and low levels (Fig. 4a, c). The southerly flow south of the frontal zone (Fig. 4g) resulted in the formation of a weak anticyclone centred over the Buenos Aires Province, La Pampa and southern Santa Fe, characterised by very weak winds (Fig. 5b). The frontal zone was intensified by the light easterly winds and coincided with the wind convergence axis at low levels and the strong humidity and temperature gradient (Fig. 5e, k).

Towards the end of the event (12Z on the 19 July), although anticyclonic conditions in the study region persisted, the frontal zone began to weaken along with the low-pressure centre in the South Atlantic and the upper-level jet stream (Fig. 4b, d, f). The pressure began to increase

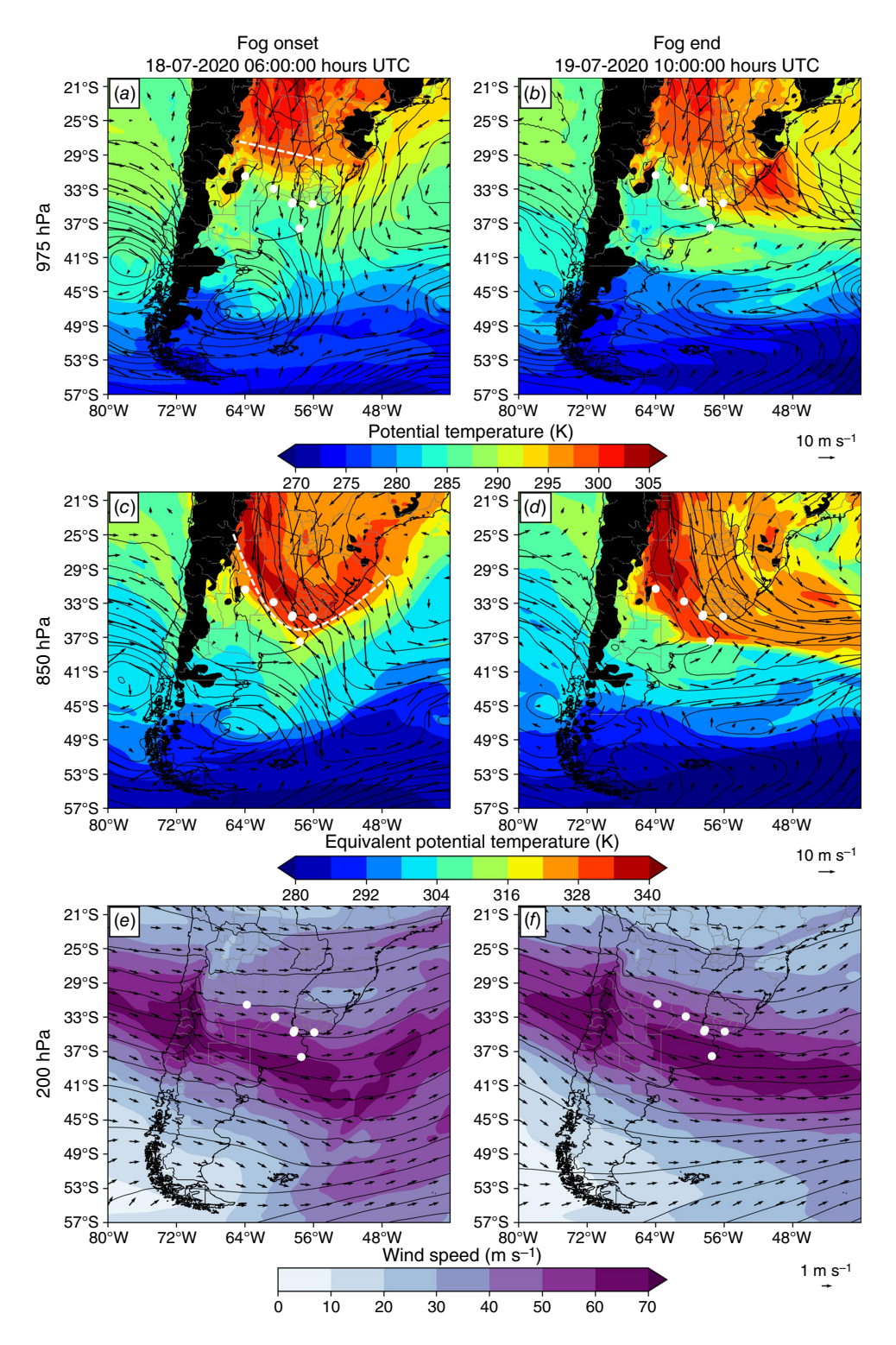


Fig. 4. Potential temperature fields at 975 hPa (*a*, *b*), the equivalent potential temperature at 850 hPa (*c*, *d*), and wind speed at 200 hPa (*e*, *f*) accompanied by the corresponding wind vectors and geopotential height (black contours) for the fog onset and fog dissipation times of the July 2020 case study. White dotted lines represent the position of the front.

slightly, although there is not a perfect match between the wind directions observed at the Ezeiza, Montevideo, Córdoba and Aeroparque airports and the reanalyses (Fig. 2). This discrepancy could be due to the difficulty of reanalyses in reproducing the fluctuation of the frontal position over time or the lack of higher spatial resolution in the reanalyses, which gives rise to uncertainty regarding the precise location of the front.

6.2. Satellite imagery

The satellite images produced with the RGB and FLS techniques shown in Fig. 6 allow discrimination between clear skies, low clouds, high clouds and deep clouds mostly during the night (Table 1). Images preceding the onset of fog in most of the airports show Buenos Aires Province, the La

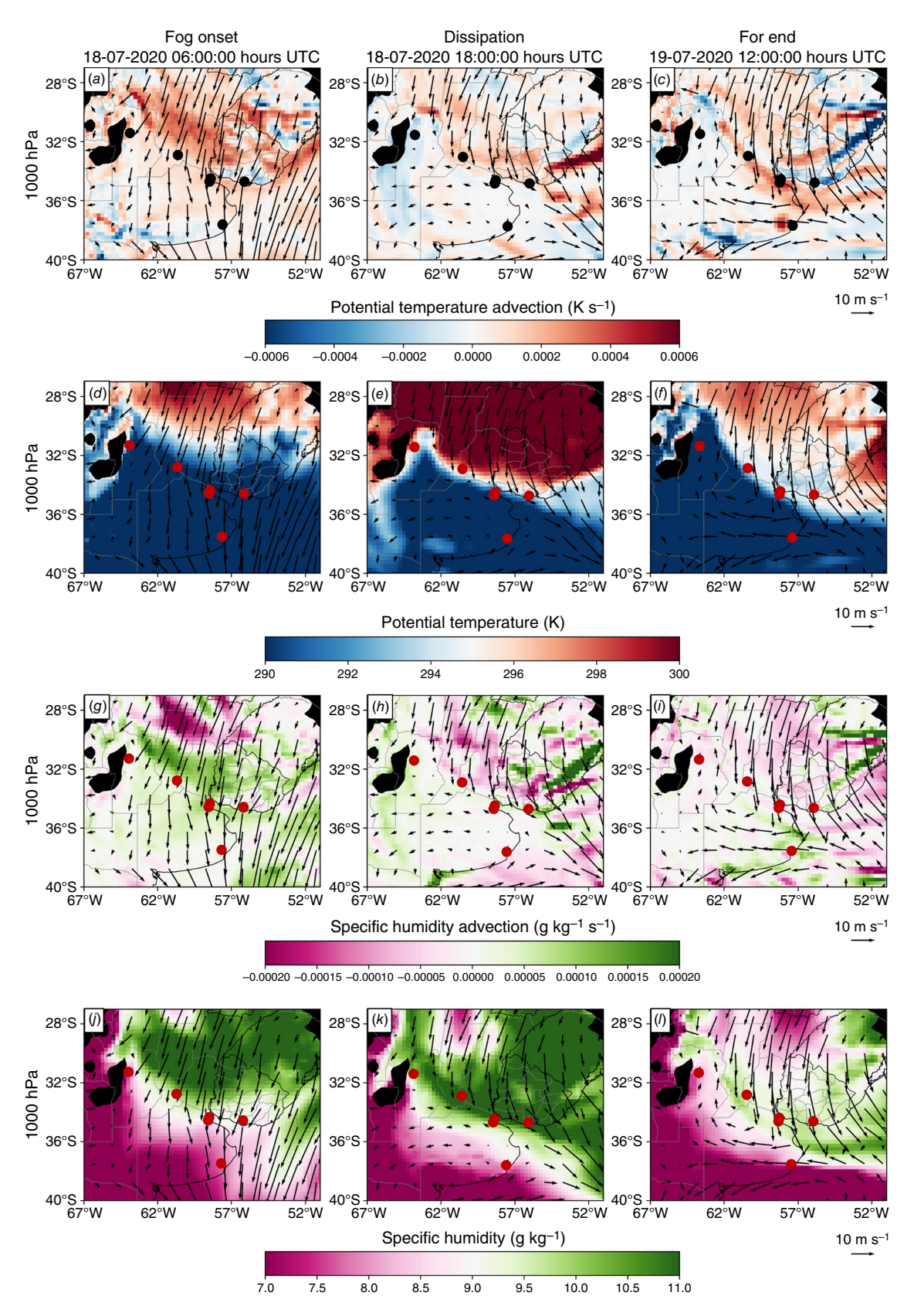


Fig. 5. Potential temperature advection fields (a-c), potential temperature (d-f), specific humidity advection (g-i), specific humidity (j-l) at 1000 hPa accompanied by the corresponding wind vectors for the times indicated at the top of each column during the July 2020 fog case.

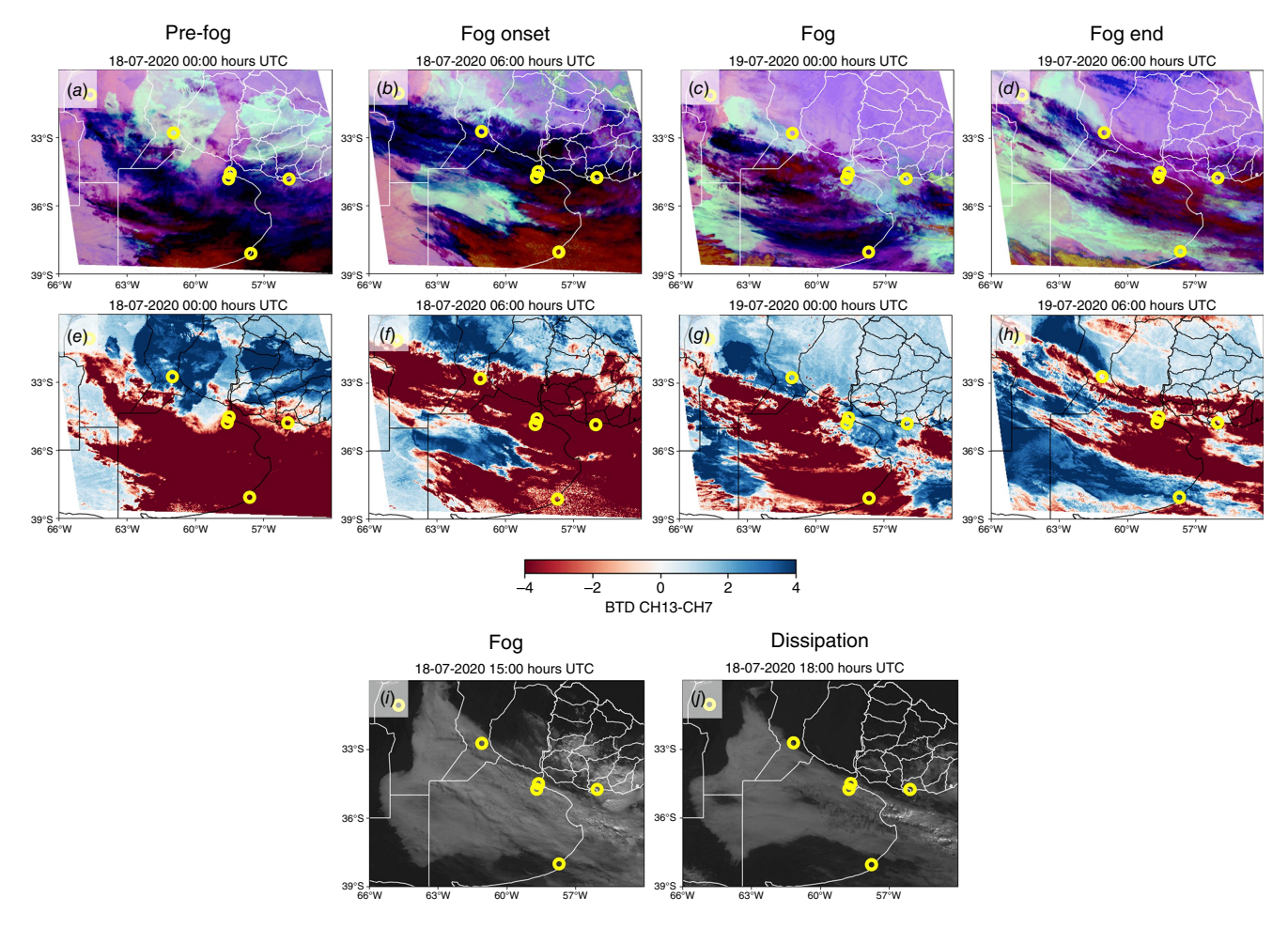


Fig. 6. Satellite images taken by the ABI sensor onboard the GOES-16 satellite for the July 2020 case study. RGB product of Night-time Microphysics (where light blue–cyan colours represent night-time fog; Table 1) (a–d). BTD (10.3–3.9 μ m) where positive values represent low clouds and fog during the night hours (e–h). Image VIS (0.64 μ m) where white shading indicates the presence of clouds and dark areas indicate clear skies (i, j).

Plata River and the sea covered by high, deep clouds (Fig. 6*a*, *e*), aligned with the baroclinic zone at 850 hPa (Fig. 4 and 5), where ascent and cloud formation occurred on the warm side of the front. North of this region, two areas of low clouds are observed – one over southern Santa Fe and western Entre Ríos provinces, and another over Uruguay (see Fig. 1).

At the start of the event (06Z), the high, deep cloudiness in the central-western Buenos Aires Province shifted eastward, following the low-to-mid-level wind direction (Fig. 4f). In the province's central region, the absence of high clouds corresponds to a dry area (Fig. 5n), revealing a new FLS area (Fig. 6b, cyan colour), though its full extent is obscured by higher clouds.

The VIS images showed no ability to distinguish areas with cloud cover before noon (15Z) because the tilt of the solar radiation beam (especially in the austral winter) generates a decrease in the reflective component perpendicular to the satellite measurement direction. During the afternoon, this technique allows one to distinguish between low clouds, identified as brighter areas, and high clouds with ice content,

identified as darker areas. VIS images during daytime on 18 July (Fig. 6i, j) illustrate the FLS coverage, which is bounded by the orography to the west near Córdoba airport. By 18Z, temporary dissipation was occurring over Córdoba, Rosario and Mar del Plata airports, while Aeroparque and Ezeiza remained under FLS cover.

At 00Z on 19 July (Fig. 6c, g), there is a reduction in the area covered by high clouds and in their thickness, while FLS coverage expands. Toward the end of the event (Fig. 6d, h), the thinning high cloud cover reveals a vast FLS area spanning Buenos Aires, La Pampa, southern Córdoba and Santa Fe provinces. The north-eastern boundary of this area aligns with the front between cold and warm air masses (Fig. 5f), placing airports on the cold side but within the reach of moisture advected from the north (Fig. 5l).

6.3. Surface observations and PBL processes

Fig. 7 displays the time series of variables reported in METAR messages for the event, and Fig. 8 presents the

time series of friction velocity, MRi and surface sensible and latent heat fluxes, alongside visibility observations for Ezeiza and Rosario airports. Additionally, this figure includes the evolution of vertical profiles for relative humidity, liquid water content, potential temperature and horizontal wind.

The passage of the warm front prior to the fog event is evident at the surface in the sustained north and north-east winds across all airports, which persisted for 24 h at Ezeiza and peaked at 21 knots in Córdoba during the latter half of 17 July (Fig. 7). Surface observations also show an upward trend in specific humidity and temperature, indicating the advection of these variables from the north (Fig. 5). Visibility started to decrease at c. 03Z on 18 July at Rosario and Córdoba airports (with precipitation at Rosario between 03Z and 06Z), whereas at Aeroparque and Ezeiza, the drop was sharper, occurring at c. 06Z on the same day (Fig. 7). At the time of reduced visibility at Ezeiza, Aeroparque, Rosario and Córdoba, there was a marked wind shift from north to east and a drop of wind speed. The disagreement between reanalysis and observations in the wind direction at this time was already pointed out during the validation and can be attributed to the anticyclonic circulation centred over Buenos Aires Province depicted in the reanalysis 4 h later (Fig. 5c) inducing weak eastern circulation over the airports mentioned. Mar del Plata and Montevideo experienced this wind shift later, at 18Z on 18 July. Fig. 5f, n indicates that, by this time, Ezeiza, Aeroparque, Córdoba and Rosario remained within a cold air mass near the surface but were starting to experience an increase in humidity, transitioning toward the characteristics of the warm air mass. This trend aligns with surface observations (Fig. 7).

As seen in Fig. 8 for Rosario and Ezeiza airports, although both stations remained on the cold side near the surface, the sloping frontal boundary allowed warmer, more humid air to overlay this cold layer. The resulting vertical turbulent mixing along the frontal surface, driven by strong vertical wind shear from c. 18Z on 17 July (Fig. 8), initiated downward turbulent moisture flux bringing down the moisture horizontally advected by the SALLJ. This effect is evident in Fig. 8c, d, where the zone of maximum liquid water content and relative humidity descends with the lowering cloud base at both airports between 18Z on 17 and 06Z on 18 July (Fig. 7). Additionally, the sharp decrease in friction velocity coincided with a reduction in visibility, signalling a decline

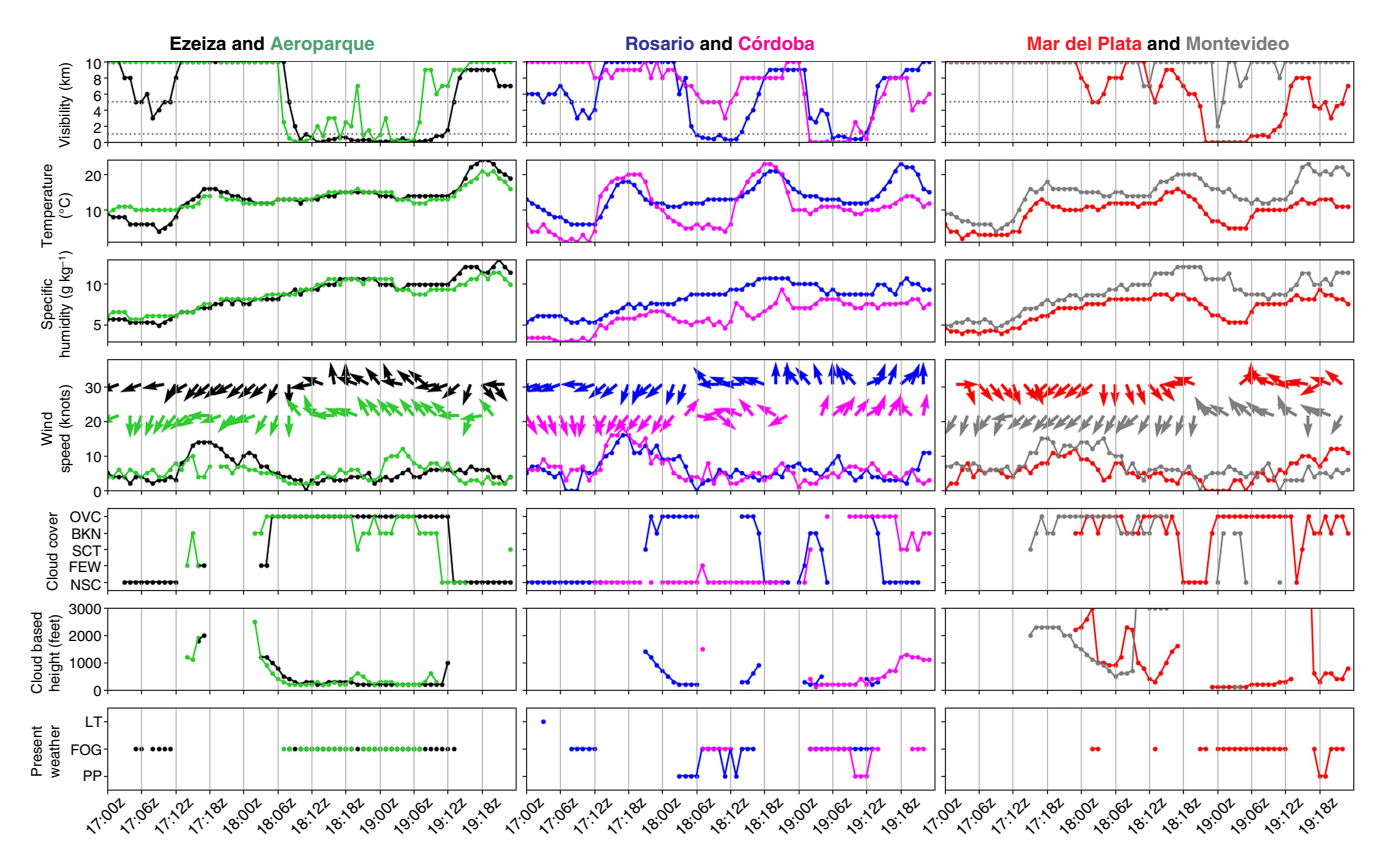


Fig. 7. Meteogram with variables reported in METAR messages for Ezeiza and Aeroparque airports (first column), Rosario and Córdoba (second column), Mar del Plata and Montevideo (third column) during the study period corresponding to the fog case of July 2020. Wind direction vectors are normalised by their speed (1 knot = 1.85 km h^{-1}). Cloud cover is encoded based on the amount of sky coverage in eighths: NSC represents the absence of significant clouds below 1500 m, FEW represents 1 and 2 eighths, SCT represents 3 and 4 eighths, BKN represents 5, 6 and 7 eighths, and OVC represents 8 eighths. METAR present weather codes were grouped into three: LT for phenomena including suspension of litometeors, FOG for fog and mist, PP for types of precipitation.

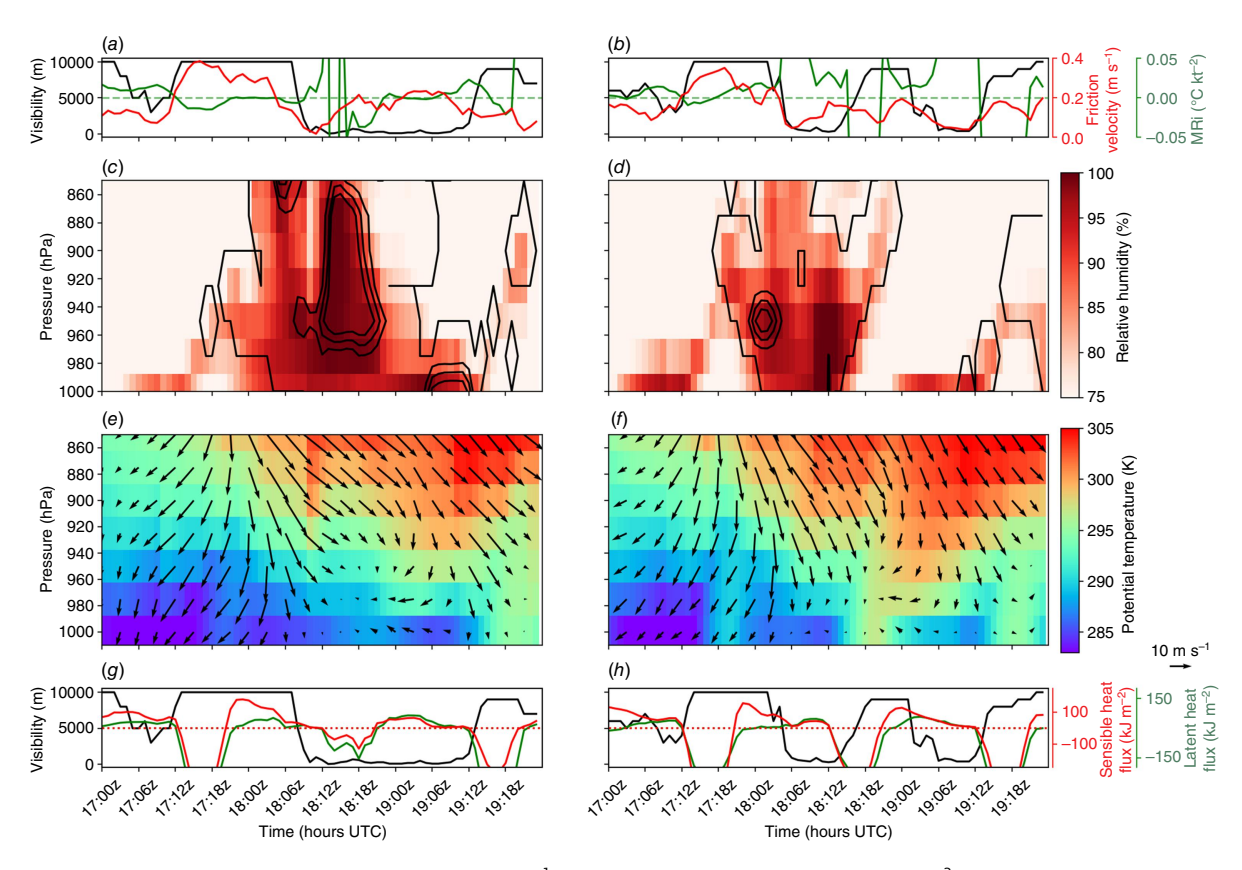


Fig. 8. Temporal evolution of friction velocity (m s⁻¹, red lines) and the MRi number (°C knot⁻², green lines) obtained from ERA5 and surface visibility (km, black lines) obtained from METARS (a, b). Vertical profile of relative humidity (shaded) and liquid water content (g kg⁻¹, black contours at intervals of 0.05 g kg⁻¹) (c, d), and vertical profile of potential temperature (shaded) and horizontal wind (vectors) (e, f) obtained from ERA5. Temporal evolution of surface sensible and latent heat fluxes (J m⁻², red and green lines) with the value 0 marked (dotted red line), and surface visibility (black lines) obtained from METARS (g, h). Panels (a, c, e) and (g) belong to the grid point closest to Ezeiza airport, whereas panels (b, d, f) and (h) correspond to Rosario airport. All plots correspond to the July 2020 study case.

in mechanical turbulence as surface wind speed diminished (see the increase in positive MRi values, indicating stabilisation). Under saturated air conditions, this reduction in turbulence is crucial for fog formation near the surface. Positive surface sensible and latent heat fluxes observed 6 h before fog formation suggest radiative cooling at the surface and a slight moisture contribution. However, the near-zero values of these fluxes at the time of the visibility drop indicate that surface processes were not the primary drivers of fog formation, supporting the hypothesis that the fog resulted from the cloud base lowering as a consequence of horizontal advection and vertical turbulent flux of moisture. Once established, the fog persisted even as turbulence levels rose again (see friction velocity from 12Z), likely owing to a stable, moist layer close to the surface that continued to provide moisture to the lower levels.

The fog dissipation period at *c*. 18Z on 18 July at Córdoba and Rosario airports is evident in observations and satellite imagery, which show these areas no longer covered by the thick cloud layer associated with the frontal surface (Fig. 6*j*). At Rosario, daytime surface heating and drying are indicated

by the negative sensible and latent heat fluxes, initiating thermal turbulence at c. 13Z on 18 July. This process resulted in the development of a convective boundary layer, characterised by a uniform potential temperature profile by 18Z (Fig. 8f). The observed surface warming and drying (evidenced by the decreasing relative humidity at 1000 hPa from 13Z in Fig. 8d) likely played a key role in fog dissipation. Although the reanalyses indicate Córdoba remained within the cold air mass (Fig. 5g), the observed increase in surface temperatures on 18 July relative to the prior day (Fig. 7) suggests a warming influence, likely because the airport was positioned on the warm side of the frontal boundary. After sunset at 21Z, clear skies facilitated radiative cooling at the surface (evidenced by the downward sensible heat flux in Fig. 8h), which led to the decoupling of the stable boundary layer and an increase in static stability, as indicated by the positive MRi (Fig. 8b). This stability suppressed the remaining turbulence (see the decreasing friction velocity), allowing a shallower fog layer to form again at c. 06Z on 19 July, though with a delay (Fig. 8d). Unlike the initial fog period in Rosario, which was driven by the cloud base lowering, this later fog

event is more connected to the daily radiative cycle (see maximum positive values in surface heat fluxes at the time of fog onset; Fig. 8h). Similar secondary fog formation was observed in Mar del Plata and Córdoba at c. 21Z on 18 July, in Montevideo at 00Z and at Aeroparque, where visibility decreased again to under 5000 m.

Ezeiza, in contrast to Rosario, experienced only brief periods of slightly negative sensible heat flux during the day due to persistent cloud cover, indicated by elevated liquid water content (Fig. 8c), observational data (Fig. 7) and satellite images (Fig. 6). Consequently, fog in Ezeiza did not dissipate during the day time and persisted into the early hours of 19 July, as deep cloud cover weakened alongside the front's progression (Fig. 4 and 5). Aeroparque, located in close proximity to Ezeiza, experienced intermittent periods of fog weakening, likely influenced by slightly stronger winds (Fig. 7) originating from the nearby river banks.

The fog eventually dissipated across nearly all airports at c. 12Z on 19 July, 1-2 h after sunrise. By this time, all airports except Mar del Plata were positioned on the warm side of the front (Fig. 5h), with the frontal cloud cover no longer affecting them (Fig. 8). Clear skies allowed radiative heating at the fog top and surface (indicated by the negative sensible and latent heat flux), which enabled thermal turbulence to disperse the fog by the end of 19 July (Fig. 7, 6 and 8c). In Aeroparque, however, fog dissipation was associated with drying from turbulent mixing induced by increasing wind speeds and clearing skies (Fig. 7). In Córdoba and Mar del Plata, this mixing instead contributed to the elevation of the fog layer (Fig. 7), forming low stratus clouds rather than dissipating the fog (Fig. 6). The latter continued being affected by slight moisture advection from the sea, contributing to the persistence of low stratus (Fig. 8).

7. January 2023 fog event

The analysis of the second fog event is analogous to the first, with Fig. 9, 10, 11, 12 and 13 reproducing mostly the same variables as Fig. 4, 5, 6, 7 and 8 respectively.

At the start of this event, there was also a baroclinic zone associated with a cold front, more notable in the fields of equivalent potential temperature at 850 hPa (Fig. 9c). This baroclinic zone is also related to the position of the jet stream at 200 hPa (Fig. 9e) and corresponds to the high and deep cloud detected in the satellite images prior to fog onset (Fig. 11a, b, e, f).

The selected airports are located over the frontal zone in the pre-fog period (Fig. 10d, j), thus explaining the large variability in the wind observed at the surface and the occurrence of precipitation during 27 January (Fig. 12). Fig. 13 allows identification of the strong vertical wind shear associated with the front at c. 950 hPa at 10Z on 27 January in Mar del Plata (Fig. 13f), where the flow has a northerly component above and a southerly component

below. On the one hand, the warm air mass is associated with a northerly flow mainly fed by the anticyclonic circulation in the Atlantic Ocean, which induces a northerly flow on its western flank and the presence of the North Argentinean Low (NAL, Seluchi et al. 2003) over northwest of the country (Fig. 9c). This circulation generates slight warm but strong moist advection at 1000 hPa over the north and east of the country (Fig. 10a) with a maximum thermal gradient crossing the Buenos Aires Province (Fig. 10e). On the other hand, the relatively cooler and drier air mass to the south-east of Buenos Aires Province is associated with a southerly flow due to the eastward displacement of the cold front at low levels. It can be seen that the greatest contrasts in the air masses at these levels are mainly associated with the difference in specific humidity and, secondly, the temperature difference (Fig. 10e, m).

The cold advection associated with the passage of the front favoured the formation of post-frontal anticyclonic circulation at low levels over the Argentine Sea, just south of Buenos Aires Province (Fig. 9b). This new circulation was responsible for the wind shift to the south-east at the airports studied (Fig. 12). Fig. 10a highlights the advective role of this wind direction, which splits the warm and moist air mass in two, leaving a relatively cooler and more humid region in the north of Buenos Aires province, south of Entre Ríos, Santa Fe and Córdoba. The cold advection is consistent with the minimum temperature observed in Ezeiza, Aeroparque, Córdob and Rosario between 06 and 12Z on 28 January (Fig. 12). In a region characterised by high specific humidity (Fig. 10j, k), the advection of colder temperatures leads to air saturation locally as it moves (Fig. 10g, h). This advection also agrees with the fog region identified in satellite images (Fig. 11b-d, f-h). In addition to the cold advection, Fig. 13 shows that the sensible heat flux and MRi in Ezeiza become slightly positive. Surface cooling contributed to generating a stable layer with weak winds, enabling the saturation of air near the surface (Fig. 13c) and the formation of fog in Ezeiza. Unlike the previous case, friction velocity did not show a significant decrease that could be related to the cessation of turbulence in the boundary layer. The evolution of surface sensible heat flux after 12Z on 28 January shows increasing turbulence (Fig. 13a) and warming (Fig. 13e) near the surface consistent with the upward sensible heat flux. This process forces the fog layer to weaken and ascend, as observed in the humidity and liquid water profile (Fig. 13c), consistent with the observations (Fig. 12).

Regarding Mar del Plata airport, Fig. 10 shows it is the first airport affected by the south-easterly and easterly flow, but with higher speeds than Ezeiza and Aeroparque airports. This airport is positioned over the convergence zone that favours a strong specific humidity gradient (Fig. 10*m*–*p*). This wind shear leads to the formation of mechanical turbulence consistent with the local maximum in friction velocity, which contributes negatively to fog formation. The cloud cover prevents strong daytime heating (see the short period

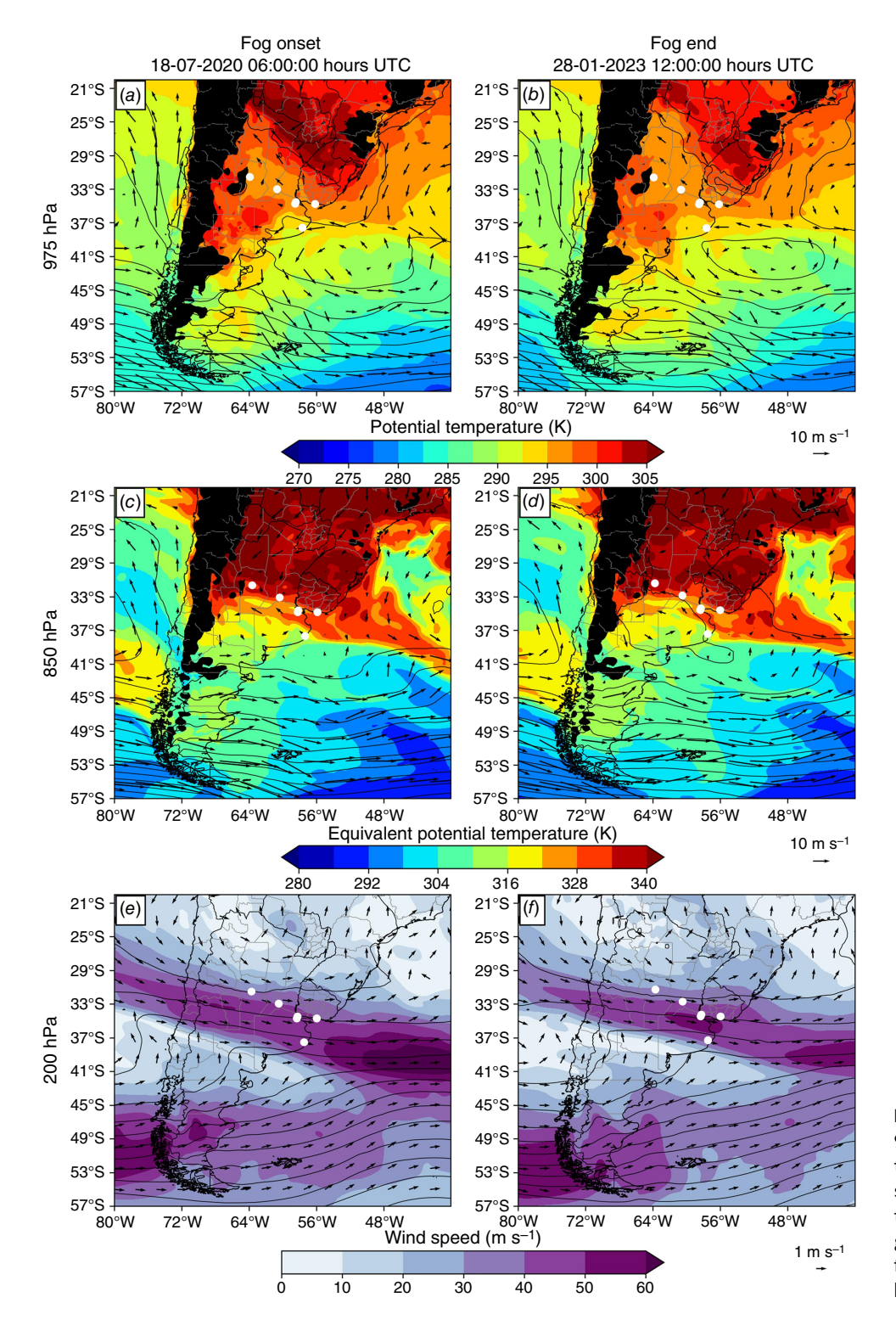


Fig. 9. Potential temperature fields at 975 hPa (*a*, *b*), the equivalent potential temperature at 850 hPa (*c*, *d*), and wind speed at 200 hPa (*e*, *f*) accompanied by the corresponding wind vectors and geopotential height (black contours) for the fog onset and fog dissipation hours of the January 2023 case study.

of upward sensible heat flux in Fig. 13h), while the east wind, sometimes more intense near the surface than at higher levels, helps to cool the entire layer below 900 hPa. During 28 January, it can be seen that the airport is immersed in the cold air mass (Fig. 10h) at low levels whose specific humidity decreases as the post-frontal anticyclone moves eastward

(Fig. 10*j*), consistent with observations (Fig. 12). By the end of 28 January and the beginning of 29th, there is a lack of high cloud cover and drying of the air except for the layer below 975 hPa (Fig. 13*d*). In this layer, cooling can be observed during the night associated with positive sensible heat flux, leading to slightly positive MRi values accompanied

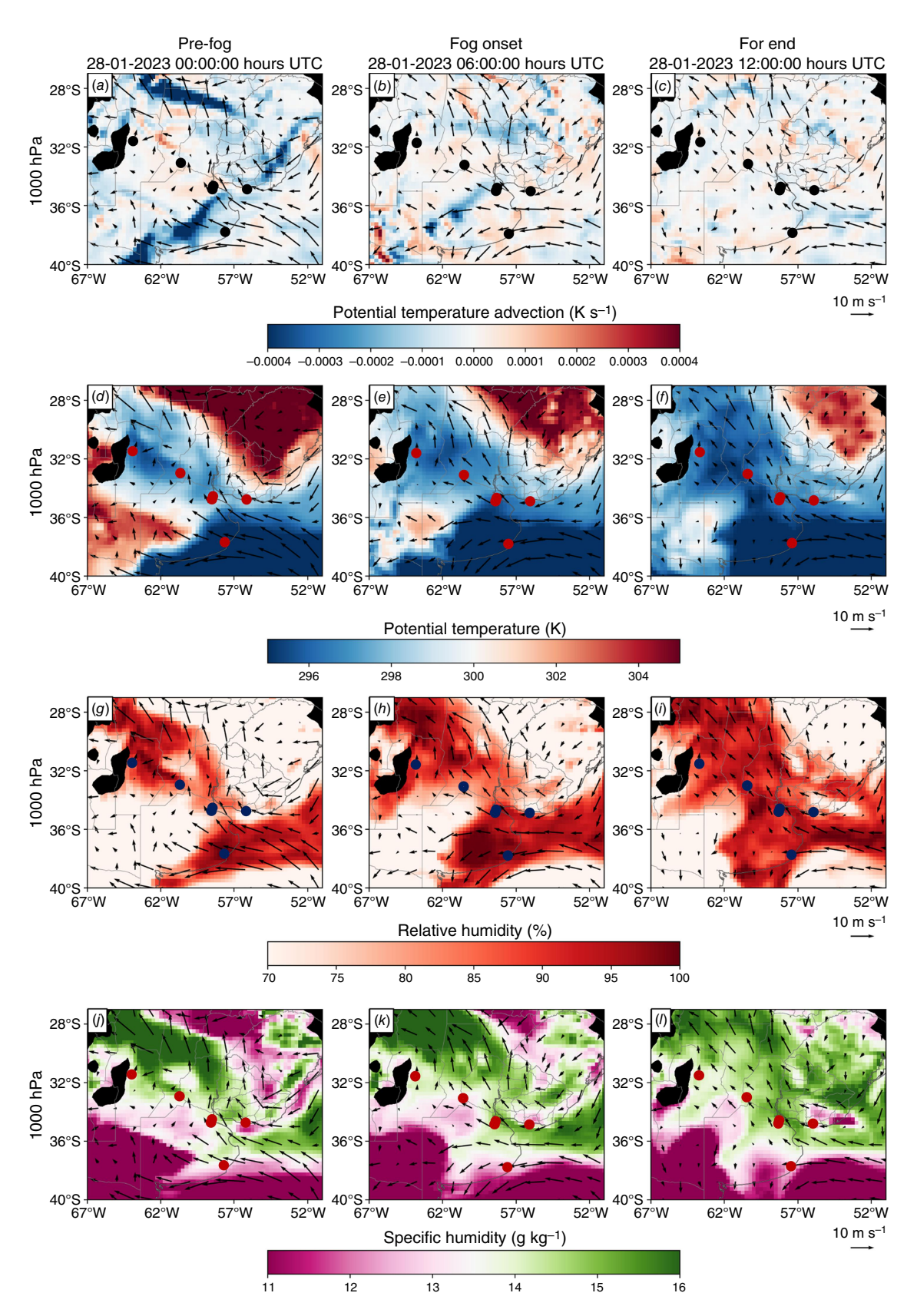


Fig. 10. Potential temperature advection fields (a-c), potential temperature (d-f), relative humidity (g-i), and specific humidity (j-l) at 1000 hPa together with the corresponding wind vectors for the times indicated at the top of each column during the January 2023 fog case.

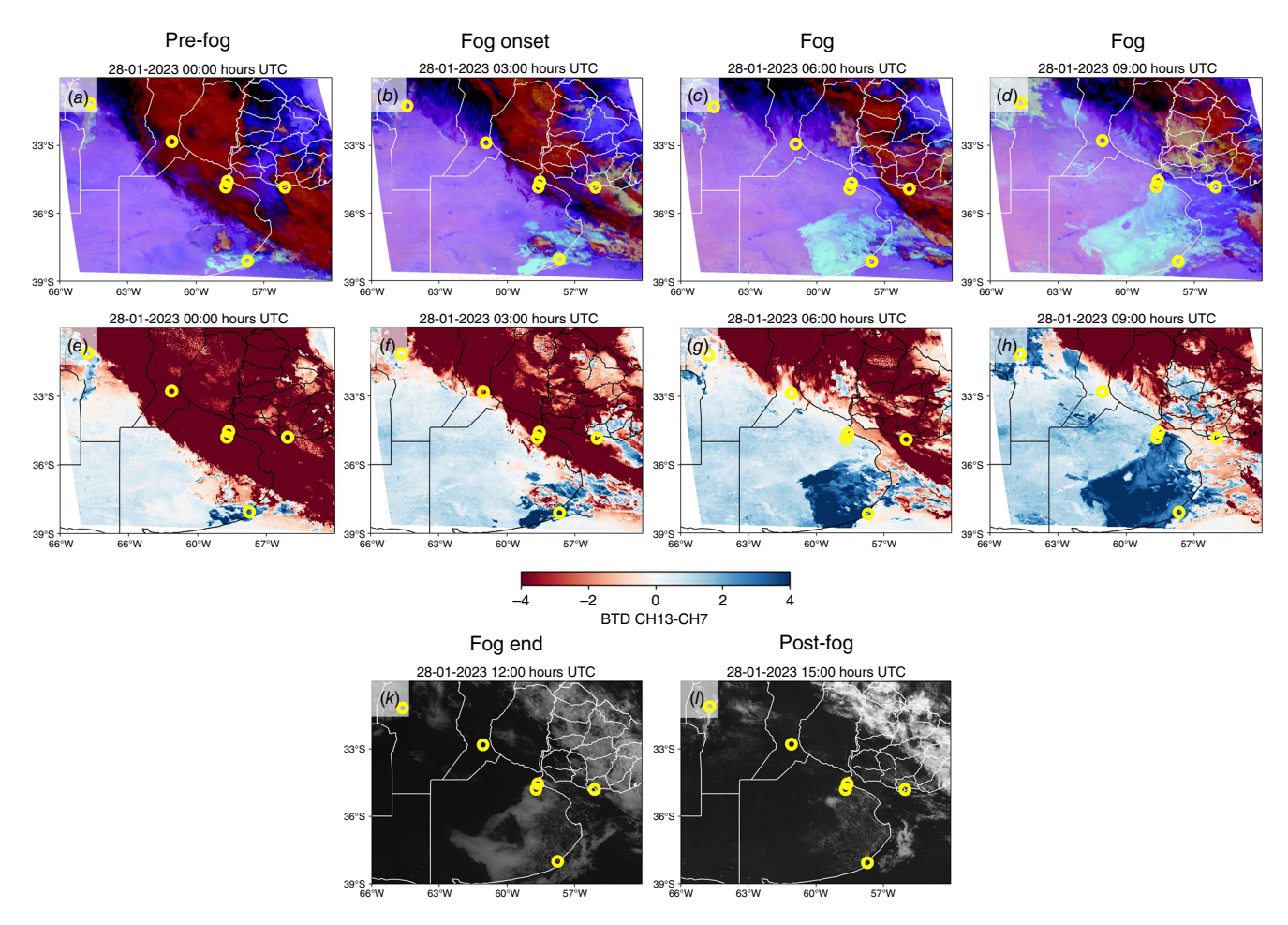


Fig. 11. Satellite images taken by the ABI sensor onboard the GOES-16 satellite for the January 2023 case study. RGB product of Night-time Microphysics (where light blue—cyan colours represent night-time fog; Table 1) (a-d). BTD (10.3–3.9 μ m) where positive values represent low clouds and fog during the night hours (e-h). Image VIS (0.64 μ m) where white shading indicates the presence of clouds and dark areas indicate clear skies (k, l).

by a decrease in turbulence (local minimum in friction velocity; Fig. 13b) at the time of fog formation (Fig. 13h). The improvement in visibility at 11Z coincides with the increase in negative sensible heat flux and MRi. The surface heating enables the formation of a convective boundary layer consistent with the increase in friction velocity and the homogenisation of the potential temperature profile at 18Z. The dissipation of fog in Mar del Plata is associated with its base drying once convective turbulence begins, while the upper layer of fog persists and is forced to ascend in the form of low clouds before eventually evaporating (Fig. 13d).

8. Discussion and conclusions

This study discusses the mechanisms influencing the life cycle of fog at major airports in Argentina, particularly during events where fog simultaneously extends across a wide region, affecting multiple airports. Two case studies from different seasons were selected, characterised by great

difficulty in forecasting and significant variability in meteorological conditions at nearby airports. To conduct this study, sets of surface and upper-air observations, GOES-16 satellite images and ERA5 reanalysis data were used. The reanalysis data were validated against available surface and upper-air observations and showed a reasonable degree of agreement with actual conditions, more accurate at height than at the surface. By contrast, satellite techniques for detecting low clouds and fog proved efficient, as there was agreement between what was observed and what was reported in the METAR, especially during night-time hours. However, the presence of overlying cloud obscures any low cloud or fog layer, limiting its use as an observational tool. Furthermore, the distinction between low cloud and fog at night and their identification during transition hours present significant challenges for these techniques.

Both fog events were associated with a baroclinic zone traversing the study region. In the first case, the primary driver was a warm front advancing from the north, whereas in the second case, a cold front dominated. Fog formation in

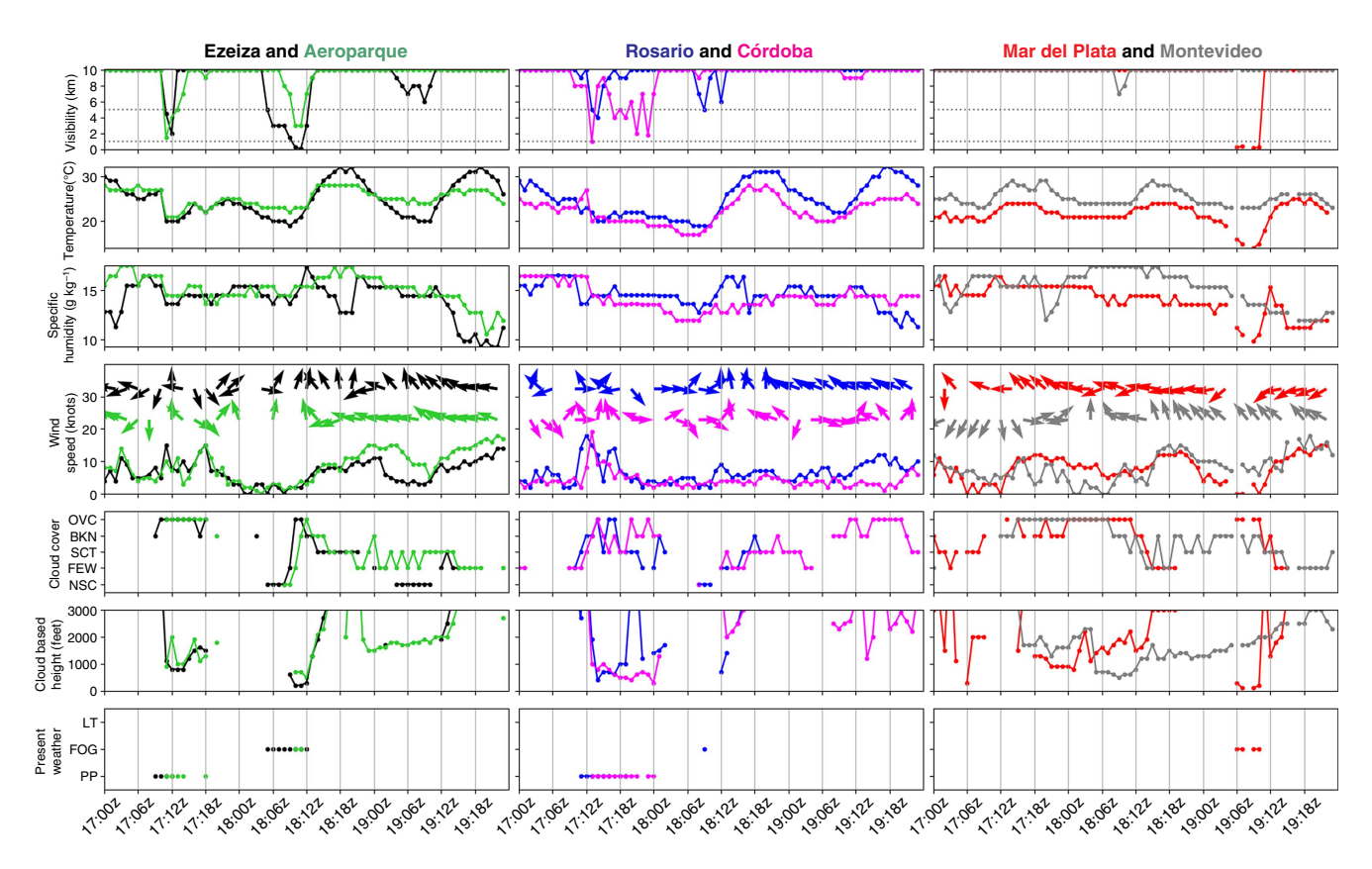


Fig. 12. Meteogram with variables reported in METAR messages for Ezeiza and Aeroparque airports (first column), Rosario and Córdoba (second column), Mar del Plata and Montevideo (third column) during the study period corresponding to the fog case of January 2023. Wind direction vectors are normalised by their speed. Cloud cover is encoded based on the amount of sky coverage in eighths: NSC represents the absence of significant clouds below 1500 m, FEW represents 1 and 2 eighths, SCT represents 3 and 4 eighths, BKN represents 5, 6, and 7 eighths, and OVC represents 8 eighths. METAR present weather codes were grouped into three: LT for phenomena including suspension of litometeors, FOG for fog and mist, PP for types of precipitation.

the first event was largely influenced by humidity advection behind the warm front, whereas in the second case, although humidity advection was a significant factor for providing a fog-favourable environment, it was the slight winds and temperature advection resulting from the postfrontal anticyclone that played a key role.

The extensive high-level cloud cover associated with the frontal system played a crucial role in the fog life cycle at each location in the first case. Fog formed at night from the advection of warm, humid air settled over a relatively cooler surface layer with lower wind speed. The vertical fluxes triggered by wind shear around the maximum wind speed led to moistening of the air near the surface. Slight nocturnal cooling and the cessation of turbulence contributed to fog formation along with the low cloud base lowering when the air near the surface became saturated. The persistence of this cloud cover also prevented the fog in Ezeiza and Aeroparque from dissipating during daytime hours, as was observed instead in Rosario and Córdoba. However, the fog reformed the following night owing to radiative cooling of the surface and the cessation of turbulence at the latter airports.

In the second case, cold advection near the surface resulting from the formation of post-frontal anticyclonic circulation along the coast of Buenos Aires province in an area with high specific humidity and calm winds combined to facilitate the formation of fog at Ezeiza and Aeroparque airports. This pattern had already been identified by regional aviation forecasters as having significant potential to generate extensive fog across the central-eastern part of the country (Yabra et al. 2021b). However, in Mar del Plata, strong winds and high cloud cover favoured the formation of low clouds rather than fog. It was not until the early morning of 29 January that clear skies, weakened surface winds and reduced turbulence allowed fog to form owing to nocturnal radiative cooling.

Fog dissipation in both events was primarily driven by turbulent mixing, initiated as the fog top layer and eventually the surface was heated by incoming solar radiation. In the first event, dissipation was mainly due to air drying and droplet evaporation. By contrast, in the second event, convective turbulent flows forced the fog to ascend, initially integrating into the low cloud cover before ultimately evaporating.

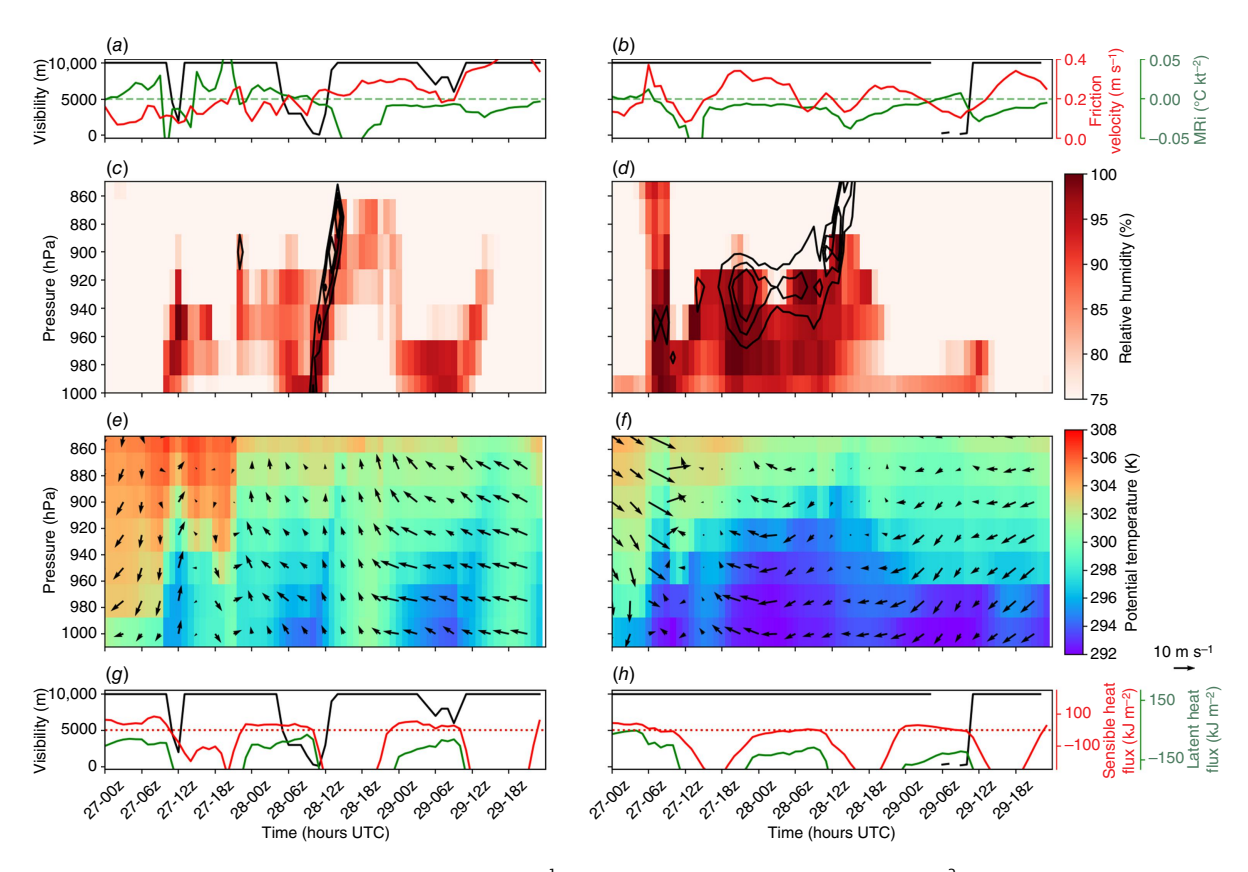


Fig. 13. Temporal evolution of friction velocity (m s⁻¹, red lines) and the MRi number (°C knot⁻², green lines) obtained from ERA5 and surface visibility (km, black lines) obtained from METARs (a, b). Time–height evolution of relative humidity (shaded) and liquid water content (g kg⁻¹, black contours at intervals of 0.05 g kg⁻¹) (c, d), and of potential temperature (shaded) and horizontal wind (vectors) (e, f) obtained from ERA5. Temporal evolution of the surface sensible and latent heat flux (J m⁻², red lines) with the value 0 marked (dotted red line), and surface visibility (black lines) obtained from METARs (g, h). Panels (a, c, e) and (g) belong to the grid point closest to Ezeiza airport, and panels (g, g, g) and (g) to Mar del Plata airport. All plots correspond to the January 2023 study case.

Although the coarse spatial and temporal resolution of the numerical model led to parameterised turbulent variables, they showed behaviour consistent with other variables and observations, enabling a qualitative analysis at smaller scales (PBL). This analysis could be improved by high-resolution numerical models and their validation using high temporal surface measurements from automatic weather stations that have started being available in some of the airports in the last year. Additionally, the evolution of MRi was also qualitatively analysed during the studied periods, revealing coherence with friction velocity and turbulent sensible and latent heat fluxes in the PBL. A climatology of events would allow the quantitative determination of MRi thresholds and ranges to characterise turbulence in the near-surface layer or for fog classification methods, as was carried out by other authors (Lin *et al.* 2022).

This study of the mechanisms driving the formation, evolution and dissipation of fog provides valuable insights into fog life cycles in the region for the first time. The findings highlight that multiple processes operating across various scales combine to influence fog behaviour. The results suggest that similar synoptic conditions can lead to

different types of fog, depending on the formation mechanisms and subsequent evolution. Cloud cover emerged as a critical factor, altering turbulent fluxes that either promote or inhibit fog formation. However, local factors, such as coastal winds or terrain friction caused by urbanisation, can lead to distinct fog development patterns even between closely situated airports under the same sky conditions. Additionally, turbulence plays a key role by modulating the stability of the PBL, ultimately influencing both the formation and dissipation of fog.

Building on this study could pave the way for developing a methodology to classify fog types specific to these airports. This classification could serve as a foundation for refining parameterisations and improving fog modelling tailored to the unique characteristics of each subregion, enhancing forecasting accuracy and operational efficiency. However, the multiplicity of mechanisms acting during the life cycle of fog in these two events does not seem to justify separating them as a classification criterion. The definition of certain thresholds for fog classification (whether using surface variables as in Tardif and Rasmussen 2007, or variables like MRi in

Lin *et al.* 2022) should be evaluated at each airport after studying the variety of mechanisms involved in most of the fog events.

References

- Amani M, Mahdavi S, Bullock T, Beale S (2019) Automatic nighttime sea fog detection using GOES-16 imagery. *Atmospheric Research* **238**, 104712. doi:10.1016/j.atmosres.2019.104712
- Andersen H, Cermak J, Fuchs J, Knippertz P, Gaetani M, Quinting J, Sippel S, Vogt R (2020) Synoptic-scale controls of fog and low-cloud variability in the Namib Desert. *Atmospheric Chemistry and Physics* **20**, 3415–3438. doi:10.5194/acp-20-3415-2020
- Baars JA, Witiw M, Al-Habash A (2003) Determining fog type in the Los Angeles basin using historic surface observation data. In 'Proceedings 16th Conference on Probability and Statistics in the Atmospheric Sciences', 12–17 January 2002, Orlando, FL, USA. J3.8. (American Meteorological Society: Long Beach, CA, USA) Available at https://ams.confex.com/ams/annual2002/webprogram/Paper29133.html
- Baker R, Cramer J, Peters J (2002) Radiation Fog: UPS Airlines Conceptual Models and Forecast Methods. In '10th Conference on Aviation, Range, and Aerospace Meteorology', 12–16 May 2002, Portland, OR, USA. 5.11. (American Meteorological Society) Available at https://ams.confex.com/ams/13ac10av/webprogram/Paper39165.html
- Beal RL, Pu Z, Pardyjak E, Hoch S, Gultepe I (2024) Evaluation of nearsurface and boundary-layer meteorological conditions that support cold-fog formation using cold fog amongst complex terrain field campaign observations. *Quarterly Journal of the Royal Meteorological Society* **150**(764), 4329–4347. doi:10.1002/qj.4818
- Bergot T, Guedalia D (1994) Numerical forecasting of radiation fog. Part I: numerical model and sensitivity tests. *Monthly Weather Review* **122**, 1218–1230. doi:10.1175/1520-0493(1994)122<1218:NFORFP>2. 0.CO:2
- Campetella C, Vera C (2002) The influence of the Andes Mountains on the South American low level flow. *Geophysical Research Letters* **29**(17), 1826. doi:10.1029/2002GL015451
- Cereceda P, Osses P, Larrain H, Farías M, Lagos M, Pinto R, Schemenauer RS (2002) Advective, orographic and radiation fog in the Tarapacá region, Chile. *Atmospheric Research* **64**(1–4), 261–271. doi:10.1016/s0169-8095(02)00097-2
- Cermak J, Bendix J (2007) Dynamical nighttime fog/low stratus detection based on Meteosat SEVIRI data: a feasibility study. *Pure and Applied Geophysics* **164**, 1179–1192. doi:11.1107/s00024-007-0213-8
- Croft PJ (2003) Fog. In 'Encyclopedia of Atmospheric Sciences'. (Eds JR Holton, JA Curry, JA Pyle) pp. 777–792. (Academic Press)
- Holton, JA Curry, JA Pyle) pp. 777–792. (Academic Press)
 Eyre JR, Brownscombe JL, Allam RJ (1984) Detection of fog at night
 using Advanced Very High Resolution Radiometer (AVHRR) imagery.
 Meteorology Magazine 113, 266–271.
- Gandhi A, Geresdi I, Gyöngyösi AZ, et al. (2024) An observational case study of a radiation fog event. Pure and Applied Geophysics 181, 2025–2049. doi:10.1007/s00024-024-03498-w
- Gultepe I, Tardif R, Michaelides SC, Cermak J, Bott A, Bendix J (2007) Fog research: a review of past achievements and future perspectives. *Journal of Pure and Applied Geophysics*, **164**, 1121–1159. doi:10.1007/s00024-007-0211-x
- Gultepe I, Pardyjak E, Hoch SWH, Fernando JS, Dorman C, Flagg DD, Krishnamurthy R, Wang Q, Gaberšek S, Creegan E, Scantland N, Desjardins S, Heidinger A, Pavolonis M, Heymsfield AJ (2021) Coastal-fog microphysics using *in-situ* observations and GOES-R retrievals. *Boundary-Layer Meteorology* **181**, 203–226. doi:10.1007/s10546-021-00622-4
- Guo L, Guo X, Luan T, Zhu S, Lyu K (2021) Radiative effects of clouds and fog on long-lasting heavy fog events in northern China. *Atmospheric Research* **252**, 105444. doi:10.1016/j.atmosres.2020. 105444
- Haeffelin M, Dupont J-C, Boyouk N, Baumgardner D, Gomes L, Roberts G, Elias T (2013) A comparative study of radiation fog and quasi-fog formation processes during the Paris Fog Field Experiment 2007. Pure and Applied Geophysics 170(12), 2283–2303. doi:10.1007/ s00024-013-0672-z

- Hersbach H, Bell B, Berrisford P, Hirahara S, Horányí A, Munoz-Sabater J, Nicolas J, Peubey C, Radu R, Schepers D, Simmons A, Soci C, Abdalla S, Abellan X, Balsamo G, Bechtold P, Biavati G, Bidlot J, Bonavita M, De Chiara G, Dahlgren P, Dee D, Diamantakis M, Dragani R, Flemming J, Forbes R, Fuentes M, Geer A, Haimberger L, Healy S, Hogan RJ, Holm E, Janiskova M, Keeley S, Laloyaux P, Lopez P, Lupu C, Radnoti G, de Rosnay P, Rozum I, Vamborg F, Villaume S, Thepaut J (2020) The ERA5 Global Reanalysis. *Quarterly Journal of the Royal Meteorological Society* **146**, 1999–2049. doi:10.1002/qi.3803
- Hu H, Huang F, Zhang S, et al. (2019) Case study of fog predictability for an event with cold-front synoptic pattern. *Journal of Ocean University of China* 18, 271–281. doi:10.1007/s11802-019-3823-8
- International Civil Aviation Organization (2016) Annex 3 to the Convention on International Civil Aviation: Meteorological Service for International Air Navigation. (ICAO) Available at https://library.wmo.int/idurl/4/49391
- International Civil Aviation Organization (2023) 'European guidance material on all weather operations at aerodromes.' (European Aviation System Planning Group November 2023)
- Keim-Vera K, Lobos-Roco F, Aguirre I, Merino C, del Río C (2024) Fog types frequency and their collectable water potential in the Atacama Desert. *Atmospheric Research* **312**, 107747. doi:10.1016/j.atmosres. 2024.107747
- Lakra K, Avishek K (2022) A review on factors influencing fog formation, classification, forecasting, detection and impacts. *Rendiconti Lincei. Scienze Fisiche e Naturali* 33, 319–353. doi:10.1007/s12210-022-01060-1
- Lapido B (2019) Estudio preliminar de nieblas en el aeropuerto de la ciudad de Rosario. BSc thesis, Departamento de Ciencias de la Atmósfera y los Océanos, Facultad de Ciencias Exactas y Naturales, Universidad de Buenos Aires, Buenos Aires, Argentina. [In Spanish]
- Li Y, Aemisegger F, Riedl A, Buchmann N, Eugster W (2021) The role of dew and radiation fog inputs in the local water cycling of a temperate grassland during dry spells in central Europe. *Hydrology and Earth System Sciences* **25**, 2617–2648. doi:10.5194/hess-25-2617-2021
- Li Y, Eugster W, Riedl A, Westerhuis S, Buchmann N, Aemisegger F (2023) Identifying key stages of radiation fog evolution using water vapor isotopes. *Agricultural and Forest Meteorology* **334**, 109430. doi:10.1016/j.agrformet.2023.109430
- Lin D, Katurji M, Revell LE, Khan B, Osborne N, Soltanzadeh I, Kremser S (2022) Fog-type classification using a modified Richardson number for Christchurch, New Zealand. *International Journal of Climatology* **43**, 314–330. doi:10.1002/joc.7761
- Liu DY, Yan WL, Yang J, Yang J, Pu MJ, Niu SJ, Li ZH (2016) A study of the physical processes of an advection fog boundary layer. *Boundary-Layer Meteorology* **158**, 125–138. doi:10.1007/s10546-015-0076-y
- Maronga B, Bosveld FC (2017) Key parameters for the life cycle of nocturnal radiation fog: a comprehensive large-eddy simulation study. *Quarterly Journal of the Royal Meteorological Society* **143**(707), 2463–2480. doi:10.1002/qj.3100
- Meyer MB, Lala GG (1990) Climatological aspects of radiation fog occurrence at Albany, New York. *Journal of Climate* **3**, 577–586. doi:10.1175/1520-0442(1990)003<0577:CAORFO>2.0.CO;2
- Petterssen S (1969) 'Introduction to Meteorology', 3rd edn. (McGraw-Hill: New York, NY, USA)
- Pilie RJ, Mack EJ, Kocmond WC, Rogers CW, Eadie WJ (1975) The life cycle of valley fog. Part I: micrometeorological characteristics. *Journal of Applied Meteorology* 14, 347–363. doi:10.1175/1520-0450(1975)014 < 0347:TLCOVF > 2.0.CO;2
- Pilié RJ, Mack EJ, Rogers CW, Katz U, Kocmond WC (1979) The formation of marine fog and the development of fog-stratus systems along the California coast. *Journal of Applied Meteorology* **18**, 1275–1286. doi:10.1175/1520-0450(1979)018 < 1275:TFOMFA > 2.
- Price JD, Lane S, Boutle IA, Smith DKE, Bergot T, Lac C, Duconge L, McGregor J, Kerr-Munslow A, Pickering M, Clark R (2018) LANFEX: a field and modeling study to improve our understanding and forecasting of radiation fog. *Bulletin of the American Meteorological Society* **99**(10), 2061–2077. doi:10.1175/bams-d-16-0299.1
- Price J, Porson A, Lock A (2015) An observational case study of persistent fog and comparison with an ensemble forecast model. *Boundary-Layer Meteorology* **155**, 301–327. doi:10.1007/s10546-014-9995-2

- Roach WT (1995a) Back to basics: fog: part 2 the formation and dissipation of land fog. *Weather* **50**, 7–11. doi:10.1002/j.1477-8696.1995.tb06053.x
- Roach WT (1995b) Back to basics: fog: part 3 the formation and dissipation of sea fog. *Weather* **50**, 80–84. doi:10.1002/j.1477-8696.1995.tb05510.x
- Roach WT, Brown R, Caughey R, Garland SJ, Readings CJ (1976) The physics of radiation fog: I a field study. *Quarterly Journal of the Royal Meteorological Society* **102**, 313–333. doi:10.1002/qj.49710243204
- Rodriguez E, Morris CS, Belz JE, Chapin E, Martin J, Daffer W, Hensley S (2005) An assessment of the SRTM topographic products. Technical Report JPL D-31639, Jet Propulsion Laboratory, Pasadena, CA, USA.
- Ruiz J, Schonholz T, Saulo C (2018) Generación de pronósticos probabilísticos de visibilidad a partir de pronósticos numéricos retrospectivos y observaciones. Visibility probabilistic forecasts based on numerical retrospective forecasts and observations. *Meteorologica* 43, 73–96. Available at http://www.meteorologica.org.ar/wp-content/uploads/2018/07/Ruiz_y-otros_Vol43N1.pdf [In Spanish with title, abstract and keywords in Spanish and English]
- Schonholz T (2015) Desarrollo de una técnica objetiva para la generación de pronósticos probabilísticos de umbrales de visibilidad empleando pronósticos retrospectivos en la estación Ezeiza. BSc thesis, Departamento de Ciencias de la Atmósfera y los Océanos, Facultad de Ciencias Exactas y Naturales, Universidad de Buenos Aires, Buenos Aires, Argentina. [In Spanish]
- Schmit TJ, Griffith P, Gunshor MM, Daniels JM, Goodman SJ, Lebair WJ (2017) A closer look at the ABI on the GOES-R series. *Bulletin of the American Meteorological Society* **98**, 681–698. doi:11.1175/BAMS-D-15-00230.1
- Seluchi ME, Saulo AC, Nicolini M, Satyamurty P (2003) The northwestern Argentinean low: a study of two typical events. *Monthly Weather Review* **131**, 2361–2378. doi:10.1175/1520-0493(2003)131 < 2361: TNALAS > 2.0.CO;2
- Tardif R, Rasmussen RM (2007) Event-based climatology and typology of fog in the New York City region. *Journal of Applied Meteorology and Climatology* **46**, 1141–1168. doi:10.1175/JAM2516.1
- Taylor GI (1917) The formation of fog and mist. Quarterly Journal of the Royal Meteorological Society 43, 241–268. doi:10.1002/qj. 49704318302
- Vasques Ferro R, Ribero C (2015) Formación de nieblas en aeroparque Jorge Newbery. In 'XII Congreso Argentino de Meteorología', 26–29

- May 2015, Mar del Plata, Argentina. (Servicio Meteorológico Nacional: Buenos Aires, Argentina) Available at http://repositorio.smn.gob.ar/handle/20.500.12160/857 [Abstract, in Spanish and English]
- Weedon GP, Osborne SR, Best MJ (2024) Dew, frost, fog and lifted temperature minima: observations in southern England and implications for modelling. *Quarterly Journal of the Royal Meteorological Society* **150**(761), 2168–2184. doi:10.1002/qj.4702
- World Meteorological Organization (1966) 'International Meteorological Vocabulary.' (WMO: Geneva, Switzerland)
- Yabra MS, de Elia R, Vidal L, Nicolini M (2021*a*) Estudio climatológico de visibilidad reducida por nieblas y neblinas en aeropuertos argentinos. Nota Técnica SMN 2021-116. Available at http://hdl.handle.net/20.500.12160/1698
- Yabra MS, de Elia R, Vidal L, Nicolini M, Vasques Ferro R, Ribero C, Chiaparri L, Fernández E, Campetella C, Bonfili O, Ceballos M, Barrera G, Troche N, López V, Schizzano M, Bentancor N, Berengua L, Steven M (2021b) Las nieblas en los aeropuertos argentinos: revisión de literatura y perspectiva de los pronosticadores. Nota Técnica SMN 2021-89. (Servicio Meteorológico Nacional: Buenos Aires, Argentina) Available at http://repositorio.smn.gob.ar/handle/20.500.12160/1540 [In Spanish with abstract in Spanish and English]
- Yabra MS, Nicolini M, Borque P, Skabar YG, Salio P (2022) Observational study of the South American low-level jet during the SALLJEX. *International Journal of Climatology* **42**(16), 9676–9696. doi:10.1002/joc.7857
- Yabra MS, de Elia R, Vidal L, Nicolini M (2023) Estudio climatológico de nieblas en aeropuertos argentinos. Fog climatology in Argentina's airports. *Meteorologica* **48**(1), e020. [In Spanish with title, abstract and keywords in Spanish and English] doi:10.24215/1850468Xe020
- Yabra MS, de Elía R, Vidal L, Nicolini M (2024) Intercomparison between METAR- and SYNOP-based fog climatologies. *Pure and Applied Geophysics* **181**, 1337–1361. doi:10.1007/s00024-024-03447-7
- Yabra MS, de Elía R, Vidal L, Nicolini M (2025) Observational characterization of fog events over the main Argentine airports. *International Journal of Climatology* e8858. doi:10.1002/joc.8858
- Zhao L, Wang W, Hao T, Qu W, Sheng L, Luo C, An X, Zhou Y (2020) The autumn haze–fog episode enhanced by the transport of dust aerosols in the Tianjin area. *Atmospheric Environment* **237**, 117669. doi:10.1016/j.atmosenv.2020.117669

Data availability. The data that support this study are available at Copernicus Climate Change Service, Climate Data Store at doi:10.24381/cds.bd0915c6, lowa Environmental Mesonet at www.mesonet.agron.iastate.edu, and in the NOAA National Centers for Environmental Information at doi:10.7289/V5WD3XVT.

Conflicts of interest. The authors declare that they have no conflicts of interest.

Declaration of funding. This work was carried out within the framework of a doctoral thesis in Atmospheric and Ocean Sciences of the Faculty of Exact and Natural Sciences of the Universidad de Buenos Aires, Argentina, based at the Servicio Meteorológico Nacional, Argentina (SMN), and funded by the Consejo Nacional de Investigaciones Científicas y Técnicas (CONICET) of the Ministry of Science, Technology and Innovation, Argentina.

Acknowledgements. The authors thank the anonymous reviewers and editor for their comments and suggestions that helped to produce a more sound and readable manuscript.

Author contributions. Melina Sol Yabra provided conceptualisation, data curation, formal analysis, investigation, methodology, data visualisation, and wrote the original and revised draft. Luciano Vidal contributed investigation, methodology, data visualisation, and wrote the original and revised draft. Matilde Nicolini provided conceptualisation, formal analysis, investigation, methodology, data visualisation, and wrote the original and revised draft.

Author affiliations

- ^ADepartamento de Ciencias de la Atmósfera y los Océanos (DCAO), Universidad de Buenos Aires (UBA), Facultad de Ciencias Exactas y Naturales (FCEN), Cc1428EGA, Buenos Aires, Argentina.
- ^BServicio Meteorológico Nacional, C1425GBE, Buenos Aires, Argentina.
- ^CConsejo Nacional de Investigaciones Científicas y Técnicas (CONICET), C1033AAJ, Buenos Aires, Argentina.
- ^DCentro de Investigaciones del Mar y la Atmósfera (CIMA), CONICET–UBA, C1428EGA, Buenos Aires, Argentina.
- EInstituto Franco Argentino Sobre Estudios de Clima y Sus Impactos (IFAECI), Unité Mixte Internationale (UMI), Centre National de la Recherche Scientifique (CNRS)—CONICET—UBA, C1428EGA, Buenos Aires, Argentina.